Acta Biomaterialia 189 (2024) 651–667

Contents lists available at ScienceDirect

Acta Biomaterialia

journal homepage: www.elsevier.com/locate/actbio

Full length article

Mitigating adverse effects of Cu-containing intrauterine devices using a highly biocompatible Cu–5Fe alloy

Lijun Yang[a,b,1], Guo Bao[b,1], Cancan Yao[a], Tian Diao[a], Zhenning Su[a], Tingting Liu[a], Guannan Li[c], Gonglei Wang[d], Xihua Chen[b], Xiangbo Xu[a,b], Bing Sun[e], Xiaoxue Xu[d,*], Bin He[a,b,**], Yufeng Zheng[a,c,**]

[a] Graduate School of Peking Union Medical College, Beijing 100730, China
[b] NHC Key Laboratory of Reproductive Health Engineering Technology Research, Department of Reproduction and Physiology, National Research Institute for Family Planning, Beijing 100081, China
[c] School of Materials Science and Engineering, Peking University, Beijing 100871, China
[d] School of Biomedical Engineering, Faculty of Engineering and Information Technology, University of Technology Sydney, NSW 2007, Australia
[e] Centre for Clean Energy Technology, School of Mathematical and Physical Sciences, Faculty of Science, University of Technology Sydney, NSW 2007, Australia

ARTICLE INFO

Article history:
Received 3 June 2024
Revised 12 September 2024
Accepted 12 September 2024
Available online 1 October 2024

Keywords:
Cu–Fe alloys
Burst release
Copper-containing intrauterine devices
Biocompatibility
Contraception

ABSTRACT

Copper-containing intrauterine devices (Cu-IUD) are adopted by worldwide women for contraception with the advantages of long-term effectiveness, reversibility and affordability. However, adverse effects occur in the initial implantation stage of Cu-IUD in uterine because of the burst release of Cu^{2+}. To minimize the burst release, in this study, we designed a series of Cu–Fe alloys with 0.5 wt%, 1 wt% and 5 wt% Fe and also further produced ultrafine grained (UFG) structure for these alloys via equal-channel angular pressing. The microstructures and properties of the coarse grained (CG) Cu, CG Cu–Fe alloys and UFG Cu–Fe alloys were systematically investigated, including grain structure and phase compositions, metallic ions release behavior, electrochemical corrosion performance, and *in vitro* cytotoxicity. With careful comparison and selection, we chose the CG Cu–5Fe and UFG Cu–5Fe for *in vivo* tests using rat model, including tissue biocompatibility, *in vivo* corrosion behavior, and contraceptive effectiveness. Moreover, the corrosion mechanism of the Cu–5Fe alloy and its improved biocompatibility was discussed. Both CG and UFG Cu–5Fe alloys exhibited dramatic suppression of Cu^{2+} release in simulated uterine fluid for the long-term immersion process. The *in vivo* tissue compatibility was significantly improved with both CG and UFG Cu–5Fe alloys implanted in the rats' uterine while the high contraceptive efficacy was well maintained. Due to the superior biocompatibility, the CG and UFG Cu–5Fe alloys can be the promising candidate material for Cu-IUD.

Statement of significance

A highly biocompatible Cu–Fe alloy was designed and fabricated for Cu-containing intrauterine devices (Cu-IUD). With 5 wt% Fe, the burst release of Cu^{2+} is inhibited due to the formed galvanic cell of Cu and Fe, resulting in earlier release of Fe^{3+}. As Fe is the most abundant essential trace element of human body, it can mitigate the toxic effects of Cu^{2+}, thus significantly improving both *in vitro* cell compatibility and *in vivo* tissue compatibility. More importantly, the Cu–5Fe alloy exhibits 100 % contraceptive efficiency as the CG Cu, but with greatly reduced adverse effects to the uterus tissues. An advanced Cu-IUD can be developed using Cu–Fe alloys.

* Corresponding author.
** Corresponding authors at: Graduate School of Peking Union Medical College, Beijing 100730, China.

E-mail addresses: Xiaoxuehelen.xu@uts.edu.au (X. Xu), hebin@nrifp.org.cn (B. He), yfzheng@pku.edu.cn (Y. Zheng).

[1] Contribute equally as first author.

https://doi.org/10.1016/j.actbio.2024.09.022

1. Introduction

The copper-containing Intrauterine Device (Cu-IUD) has been widely used for female contraception with the advantages of high effectiveness, long-lasting lifetime and affordability [1–3]. Its contraceptive mechanism involves a sterile inflammatory response in the uterine cavity [4–7], interferences with sperm motility by released Cu^{2+} [8], and potential toxicity effect of Cu^{2+} to embryos [9]. However, initial implantation of Cu-IUD can cause side effects like pelvic inflammatory disease, menstrual irregularities, or uterine perforation [10–12], attributed to the burst release of Cu^{2+} from the freshly implanted Cu-IUD [13].

Efforts of mitigating these side effects while maintaining the Cu-IUD's efficacy have led to the design and development of alternative materials. Nanocomposites, such as $CuCl_2/SiO_2$/PVA, were designed, and the reduced burst release of Cu^{2+} as well as the uterine bleeding were achieved. However, the low mechanical properties affected the long-term usage of the IUD [14–16]. Another Cu nanocomposite with Cu micro/nanoparticles in the dense or porous Low-Density Polyethylene (Cu/LDPE) inhibited initial Cu^{2+} release, but exhibited very low long-term Cu^{2+}release [17–19]. Furthermore, surface modifications with anti-inflammatory drugs on Cu-IUD helped severe bleeding reactions but induced issues with drug burst release [20].

Bulk metals and alloys with refined structure and/or varied compositions are being explored for IUDs. Ultrafine grained Cu (UFG Cu) with uniform grains less than 1 μm presented enhanced mechanical properties, well-maintained contraceptive efficacy and greatly reduced Cu^{2+} burst release to 160 μg/day [21]. To further eliminate the burst release of Cu^{2+}, electrochemically active alloy elements like Mg and Zn were alloyed into Cu to suppress Cu corrosion via anodic sacrificial method [22]. The Cu–0.4Mg alloys with coarse grained structure and ultrafine grained structure were developed and investigated as the active materials for Cu-IUD [24]. The addition of 0.4 wt% Mg into Cu exhibited significant improvement in the cell compatibility and obviously decreased burst release of Cu^{2+} from the early corrosion of Mg. Moreover, Cu–38 Zn alloys were also studied and demonstrated very much reduced Cu^{2+} owing to the high concentration of Zn [23,24]. The Cu^{2+} burst release was alleviated to a great extent with these purposely-designed alloys, but completely mitigating burst release is still the goal of developing more Cu alloys.

Iron (Fe) is another promising alloy element due to its lower electrochemical potential and high biocompatibility. The standard electrode potential of Fe is lower than that of Cu, making it more susceptible to oxidation, hence reducing the corrosion rate of Cu [25]. Moreover, Fe is the most abundant essential trace element in the human body, involved in oxygen transport and storage, metalloenzymes synthesis, hematopoietic function, and immune function. The Fe content in the human body is around 4 g [26], and its concentration in human serum is higher than 0.1 mmol/L [27]. Since the physiological baseline concentration of Fe in the body is relatively high, the threshold for Fe^{3+} to cause systemic toxicity is also high [28]. In addition, adding Fe to biodegradable metal implants may serve as a supplement to the human body [25]. Cardiovascular stents made of Fe-based alloys demonstrated satisfied biocompatibility, without any local or systemic toxicity [29].

In this work, we developed a series of Cu–Fe alloys for Cu-IUD. Following the Cu–Fe binary alloy phase diagram and the solubility of Fe in Cu [30], three different compositional Cu–Fe alloys were fabricated, Cu–0.5wt%Fe, Cu–1 wt%Fe and Cu-5 wt%Fe. Furthermore, we prepared ultra-fine grained (UFG) Cu–Fe alloys via equal-channel angular pressing (ECAP). We compared the microstructure, corrosion performance, *in vitro* and *in vivo* biocompatibility, contraceptive effectiveness of the coarse grained (CG) Cu–Fe alloys and the UFG Cu–Fe alloys with pure CG Cu as the control. The feasibility of Cu–Fe alloys for Cu-IUDs was comprehensively evaluated, along comparisons with other developed IUD Cu alloys.

2. Materials and methods

2.1. Materials

The pure CG Cu ingot (diameter (d)=10 mm, 99.99 %) was purchased from Yunnan Kuntong Co. Ltd., China. The Cu–Fe alloys ingots with the diameter of 100 mm and length of 100 mm, including CG Cu–0.5Fe, CG Cu–1Fe, and CG Cu–5Fe (all were weight percentage, wt%), were manufactured in the Hunan Rare-Earth Material Research Institute, China. The CG Cu–Fe alloys underwent equal-channel angular pressing (ECAP) for 8 passes to obtain ultrafine-grained alloy structures and were labeled UFG Cu–0.5Fe, UFG Cu–1Fe and UFG Cu–5Fe.

The experimental specimens were cut into circular discs (d = 10 mm, thickness (t)=2 mm) or cylinders (d = 1.5 mm, L = 10 mm). The circular discs were ground using the SiC sandpaper with grits of 400, 800, and 2000, then sonicated in anhydrous ethanol for 15 min and air dried. For the microstructure observation, the discs were further polished with 3 μm and 50 nm SiO_2 suspension in sequence, followed by final surface polishing using a Gatan PECS II ion miller. Once mirror-smooth, the discs were etched with an etchant solution, rinsed with Milli-Q water, and dried with an N_2 gun. The prepared discs were examined using a Zeiss Supra 55VP Scanning Electron Microscopy.

2.2. Electrochemical measurement

The circular discs were used in the electrochemical measurements. The Simulated Uterine Fluid (SUF) was prepared in the following compositions: $NaHCO_3$ (0.25 g/L), $NaH_2PO_4{\cdot}2\ H_2O$ (0.072 g/L), $CaCl_2$ (0.167 g/L), KCl (0.224 g/L), NaCl (4.97 g/L) and glucose (0.5 g/L) [31–33]. The pH of the SUF was adjusted to 7.0. An electrochemical workstation (Autolab, Metrohm, Switzerland) was used with a three-electrode system consisting of a platinum sheet auxiliary electrode (counter electrode), a saturated calomel electrode (reference electrode), and the working electrode (sample). The exposed surface area of the alloys to the SUF was 0.196 cm^2. Open-circuit potential measurements were carried out for 3600 s, followed by the Potentiodynamic polarization tests at a scan rate of 1 mV/s. The experimental data were analyzed using Nova 1.11 software, and the corrosion potential (E_{corr}) and corrosion current density (i_{corr}) were calculated through Tafel analysis of the polarization curves.

2.3. Long-term immersion test

Long-term immersion experiments were conducted using the prepared circular discs (d = 10 mm, h = 2 mm) of the 7 alloys in SUF with a solution volume-to-sample surface area ratio of 20 mL/cm^2. Following the ASTM G31-72 standard, the solution temperature was kept at 37 ± 0.1 °C. Five parallel discs were utilized for each alloy, and each disc was weighed and recorded. The immersion time points were set at 1, 10, 20, 30, 45, 60, 90, 120, 150, 180, 210, 240, 270, and 300 days. At each time point, SUF was replaced, and the pH of the used SUF was measured using a pH meter. The concentrations of Cu^{2+} and Fe^{3+} in the SUF were determined using an Inductively Coupled Plasma Atomic Emission Spectrometer (ICP-AES, iCAP6300, Thermo). The released concentration rates of the Cu^{2+} and Fe^{3+} was then converted to an exposure surface area of 200 mm^2 for direct comparison with the released rate of Cu^{2+} from typical Cu-IUD200 [32,34]. At each time point of the 1st, 10th, 30th, 60th, 150th, and 300th day of immersion, the immersed discs of each alloy were taken out, rinsed with deionized

water to clean the sample surface, and air-dried at room temperature. Four samples were treated with concentrated sulfuric acid to remove corrosion products, followed by deionized water rinse. The discs were weighted after these were completely dried in air. The corrosion rates of the CG Cu, CG Cu–Fe alloys and UFG Cu–Fe alloys in SUF were calculated using the following formula:

$$C = \frac{\Delta m}{\rho \times A \times t}$$

Where C is the corrosion rate in mm/year, Δm is the weight loss of the discs before and after immersion in SUF (mg), ρ is the density of the disc (g/cm^3), A is the surface area of the disc exposed to SUF (mm^2), and t is the immersion time of the sample in SUF (year).

2.4. Corrosion morphology observation and corrosion product composition analysis

The corrosion morphology of the alloy surface and the composition of the corrosion products were analyzed using one of the immersed discs from each alloy group. The morphology of the alloy surface was imaged using a scanning electron microscope (SEM, S-4800, Hitachi, Japan). Energy dispersive X-ray spectrometer (EDX, Quanta 200FEG, FEI) was adopted to analyze the elemental composition of the corrosion products. The phase composition of the products was analyzed using a Cu Kα radiation X-ray diffractometer (XRD, DMAX2400, Rigaku) with the following conditions: tube voltage of 40 kV, tube current of 100 mA, scan range of 20–80° and scan step of 0.02°.

2.5. In vitro studies on biocompatibility of alloys

2.5.1. Sample preparation

Circular thin discs (d = 10 mm, h = 2 mm) were used. The discs were subjected to UV irradiation for 30 min on each side for sterilization. The discs were placed in the complete cell culture medium with a solution volume-to-sample surface area ratio of 1.25 cm^2/mL at 37 °C for 24 h. After 24 h, the extract solution was collected, labeled, and centrifuged (1000 rpm, 5 min) to obtain the supernatant for further use.

2.5.2. Cell culture

Human endometrial stromal cells (HESC) were purchased from the American Type Culture Collection (ATCC), human endometrial epithelial cells (HEEC) were purchased from Bnbio Company (Beijing, China), and human umbilical vein endothelial cells (HUVEC) were obtained from the National Experimental Cell Resource Sharing Platform. HEEC and HESC were cultured in Dulbecco's Modified Eagle Medium/Nutrient Mixture F-12 (DMEM/F12, Gibco, USA) supplemented with 10 % fetal bovine serum (FBS, Gibco, Australia), 100 U/mL penicillin, and 100 μg/mL streptomycin (Gibco, USA). HUVEC was cultured in Endothelial Cell Medium (ECM, ScienCell, USA) supplemented with 10 % fetal bovine serum, 100 U/mL penicillin, 100 μg/mL streptomycin and 1 % Endothelial Cell Growth Supplement. The cells were maintained in a humidified atmosphere at 37 °C with 5 % CO_2.

2.5.3. Cytotoxicity test

The cytotoxicity of the seven metallic materials, CG Cu, CG Cu–0.5Fe, CG Cu–1Fe, CG Cu–5Fe, UFG Cu–0.5Fe, UFG Cu–1Fe, and UFG Cu–5Fe, was evaluated using the cell lines of HEEC, HESC and HUVEC. Cells were seeded into 96-well plates with a density of 1×10^4 cell/well and cultured at 37 °C with 5 % CO_2 for 24 h. Negative control was the cells that were cultured in complete culture medium without any extract. Positive control was the cells that were treated with 10 % DMSO, and the blank control was the complete culture medium without cells. Experimental groups were the cells cultured in the complete culture with 100 %, 50 %, 10 % of extract (200 μL/well) for 1, 2, and 3 days. At each time point, the culture medium from each well was removed and 100 μL fresh culture medium containing 10 % CCK-8 reagent (Dojindo, Japan) was added to each well for a further 2 h culture at 37 °C. The absorbance value of the cell culture medium in each well was measured at 450 nm using a microplate reader (Bio-Rad 680). The experiment was performed in triplicate with five duplicates for Cu and each Cu–Fe alloy.

2.5.4. Transcriptomic cell treatment

As the HESC makes up the largest proportion of uterine tissue cells, we subsequently conducted transcriptomic analysis on HESC for the CG Cu and CG Cu–5Fe. HESC was seeded into 6-well plates and cultured until it reached 80 %–90 % confluence. The extract from the CG Cu and CG Cu–5Fe was collected and diluted to 50 % with complete culture medium (89 % DMEM/F12 + 10 % FBS + 1 % penicillin-streptomycin). For the experimental group, cells were treated with the 50 % concentrated extract of the CG Cu and CG Cu–5Fe for 12 h, respectively, while the negative control group only with 100 % complete culture medium, Three replicates for each group.

2.5.5. RNA extract, library construction and sequencing

Total RNA was extracted using Trizol reagent kit (Invitrogen, Carlsbad, CA, USA) according to the manufacturer's protocol. RNA quality was assessed on an Agilent 2100 Bioanalyzer (Agilent Technologies, Palo Alto, CA, USA) and checked using RNase free agarose gel electrophoresis. After total RNA was extracted, eukaryotic mRNA was enriched by Oligo(dT) beads. Then the enriched mRNA was fragmented into short fragments using fragmentation buffer and reversely transcribed into cDNA by using NEBNext Ultra RNA Library Prep Kit for Illumina (NEB #7530, New England Biolabs, Ipswich, MA, USA). The purified double-stranded cDNA fragments were end repaired, A base added, and ligated to Illumina sequencing adapters. The ligation reaction was purified with the AMPure XP Beads(1.0X). Ligated fragments were subjected to size selection by agarose gel electrophoresis and polymerase chain reaction (PCR) amplified. The resulting cDNA library was sequenced using Illumina Novaseq6000 by Gene Denovo Biotechnology Co. (Guangzhou, China). The sequencing results were analyzed using bioinformatics methods, including GO (Gene Ontology) Enrichment Analysis, Pathway Enrichment Analysis.

2.6. In vivo studies on biosafety and contraceptive efficiency

2.6.1. Sample preparation

Cylindrical samples (d = 1 mm, L = 10 mm) were ground using the 400, 800, and 2000 grit SiC sandpapers. They were then sonicated in anhydrous ethanol for 15 min and air-dried at room temperature on lint-free paper. At one end of the material, a groove was created and a sterile surgical suture (5#) was fixed in the groove to secure the sample inside the rat uterus. The sutured sample was placed in a 12-well plate and subject it to UV irradiation for 30 min on each side for sterilization.

2.6.2. Animal care

Adult Sprague-Dawley (SD) rats, both females and males, 8–9 weeks old and the average weight of 200–230 g, were obtained from the Beijing Vital River Laboratory Animal Technology Co. Ltd (Beijing, China). The rats were housed and maintained according to standard protocols. They had free access to sterile water and conventional food. All rats were allowed to acclimate for one week before experiment was conducted. All animal care and treatment

protocols were approved by the Ethical Committee of the National Research Institute for Family Planning.

2.6.3. Implantation

Sixty female SD rats were randomly divided into 5 groups: normal control group ($n = 12$), sham surgery group ($n = 12$), CG Cu group ($n = 12$), CG Cu-5Fe group ($n = 12$), and UFG Cu-5Fe group ($n = 12$). The normal control group received no treatment. The sham surgery group underwent the entire surgical procedure without implantation of any sample. The alloy implantation groups had CG Cu, CG Cu–5Fe, and UFG Cu-5Fe implanted into the right uterine cavity of the rats. There were 4 time points of 3, 7, 14, and 28 days implantation with 3 rats at each time point. Throughout the experiment, the rats were examined daily to ensure their health status.

2.6.4. Histological analysis

After 3, 7, 14, and 28 days implantation, uterine tissues directly contacting with the implanted alloys were harvested from the material implantation groups and fixed in 4 % (w/v) paraformaldehyde (Sigma-Aldrich, USA). After fixation, the samples were processed for embedding and staining following the methods described in the referenced articles [23,24]. In brief, the samples were dehydrated through a series of ethanol gradients (70 %, 75 %, 80 %, 95 % I and II, and 100 % I and II), followed by xylene I and II, and paraffin I and II. After embedding in paraffin, the tissues were sectioned into 5 μm thick slices, which were then mounted on adhesive slides. The slides were baked at 65 °C for 1.5 h, followed by dehydration through a series of ethanol gradients (100 % I and II, 95 % I and II, 80 %, and 75 %) and staining with hematoxylin and eosin (H&E). The H&E-stained uterine tissue sections were observed and imaged using an optical microscope.

2.6.5. Corrosion morphology observation of the implanted Cu and Cu–Fe alloys

The Cu and Cu–Fe alloy cylinders were collected after 3, 7, 14, and 28 days implantation. Corrosion morphology and corrosion products of the alloys were analyzed through SEM, EDX, XRD, and X-Ray Photoelectron Spectroscopy (XPS, Axis Ultra Analytical, Great Britain) with Al Kα radiation as the excitation source. The binding states between different elements were determined through high-resolution narrow scans. The calibration of binding energy shifts that occurred during the testing process was performed using the characteristic energy peak C 1s (284.8 eV) of the carbon source. The composition and chemical states were analyzed using Avantage software.

2.6.6. Antifertility experiment

To evaluate the contraceptive effect of the Cu and Cu–Fe alloys, 80 sexually mature female SD rats and 20 male SD rats were used in this experiment. The female rats were randomly divided into 5 groups: normal control group ($n = 10$), sham surgery group ($n = 10$), CG Cu group ($n = 20$), CG Cu–5Fe group ($n = 20$) and UFG Cu–5Fe group ($n = 20$). The normal control group received no treatment. The sham surgery group underwent the entire surgical procedure without implantation of any material in the rat uterine cavity. In the material implantation groups, CG Cu, CG Cu–5Fe, and UFG Cu–5Fe alloys were implanted into the right uterine cavity of the female rats. After a recovery period of two weeks, the female rats were mated with the male rats. The female rats were evaluated for the presence of vaginal plugs in the following morning, and the day on which the vaginal plug was observed was recorded as gestation day 0.5. On gestation day 11.5, the rats were sacrificed, and the number of embryos in the left and right uterine horn was examined and recorded.

2.7. Statistical analysis

In this study, the data are shown as the mean values ± standard deviation. The statistical difference was analyzed using the unpaired t-test and defined it as significant differences when $p < 0.05$.

3. Results

3.1. Microstructures of the CG Cu and CG/UFG Cu–Fe alloys

The grain and phase microstructures of the CG Cu and Cu alloys were observed using SEM after the polishing and surface etching. In Fig. 1, the CG Cu exhibited uniform single-phase structure with grains in geometric shapes. The grain size ranges from 2 μm to 25 μm. After the addition of 0.5 % and 1 % Fe into the pure Cu matrix, uniform single-phase structure with large grains up to millimeters were observed and the grain boundary continues in a long distance and separates the grains in different crystal orientations indicated by the varied etching morphologies. It is worth noting that the CG Cu–5Fe alloy presented two distinguished phases with the dominate grains in the size of 50–250 μm. The second phase in the size of 5–10 μm was dark and scatters in the Cu matrix. EDX was performed on both the dark phase and the surrounding matrix. The EDX spectrum of the dark phase presented much high Fe content (~80 wt%) than Cu (~10 wt%) while the surrounding areas showed the absence of Fe. The Cu–Fe alloys after ECAP process showed much fine grains compared to the CG Cu–Fe alloys. Both the UFG Cu–0.5Fe and UFG Cu–1Fe displayed single-phase structure with elongated and thin grains (1–2 μm in width and ~10 μm in length). Similar to the CG Cu–5Fe, there were two phases presenting in the narrow and long grains microstructure of the UFG Cu–5Fe alloy. The EDX spectrum on the dark phase presented 79.0 wt% Fe and 9.2 wt% Cu, suggesting the Fe-rich phase. The Fe-rich phases were further confirmed via EDX elemental mapping results shown in Fig. S1.

3.2. The release rates of Cu^{2+} and Fe^{3+} in SUF for 300 days

Fig. 2 presents the release rates of Cu^{2+} and Fe^{3+} from the CG Cu and CG/UFG Cu-Fe alloys in SUF at 37 °C for 300 days. In Fig. 2A, the CG Cu and CG/UFG Cu–0.5/1Fe alloys exhibited higher Cu^{2+} release rates during the first month, indicating a burst release. As shown in Fig. 2B, the initial Cu^{2+} release from day 1 to day 30 peaked on the 2nd day at 251.4 μg/day for CG Cu, 206.9 μg/day for UFG Cu–0.5Fe, and 286.9 μg/day for CG Cu-1Fe. After 30 days, the Cu^{2+} release rates gradually decreased, peaking again on the 180th day at 88.0 μg/day for UFG Cu-0.5Fe and 55.8 μg/day for UFG Cu-1Fe. The release rates for CG Cu and CG Cu–0.5/1Fe alloys fell between these values, eventually stabilizing at 4–15 μg/day.

For the alloys with 5 % Fe, the UFG Cu-5Fe alloy showed a Cu^{2+} burst release on the 6th day of immersion in the SUF (181.9 μg/day) and 9th day (207.2 μg/day). In contrast, the CG Cu-5Fe alloy exhibited exceptionally steady Cu^{2+}release with slight fluctuations in the first 10 days (maximum 43.9 μg/day) and a consistent release rate at 2.0 μg/day thereafter (Fig. 2B). The CG Cu–5Fe presented an ideal release of Cu^{2+} with no initial burst release but a sustained release over long term for contraceptive efficacy [22,35].

Fig. 2C&D shows the Fe^{3+} release rates of the Cu–Fe alloys. The alloys with low Fe content, both CG/UFG Cu–0.5Fe and CG/UFG Cu–1Fe, had very low Fe^{3+} release rates (as low as 0.005 μg/day). On the contrary, both the CG Cu–5Fe and UFG Cu–5Fe alloys exhibited significantly higher Fe^{3+} release rates, 627.3 μg/day and 316.0 μg/day, respectively, in the early stage of immersion. Such

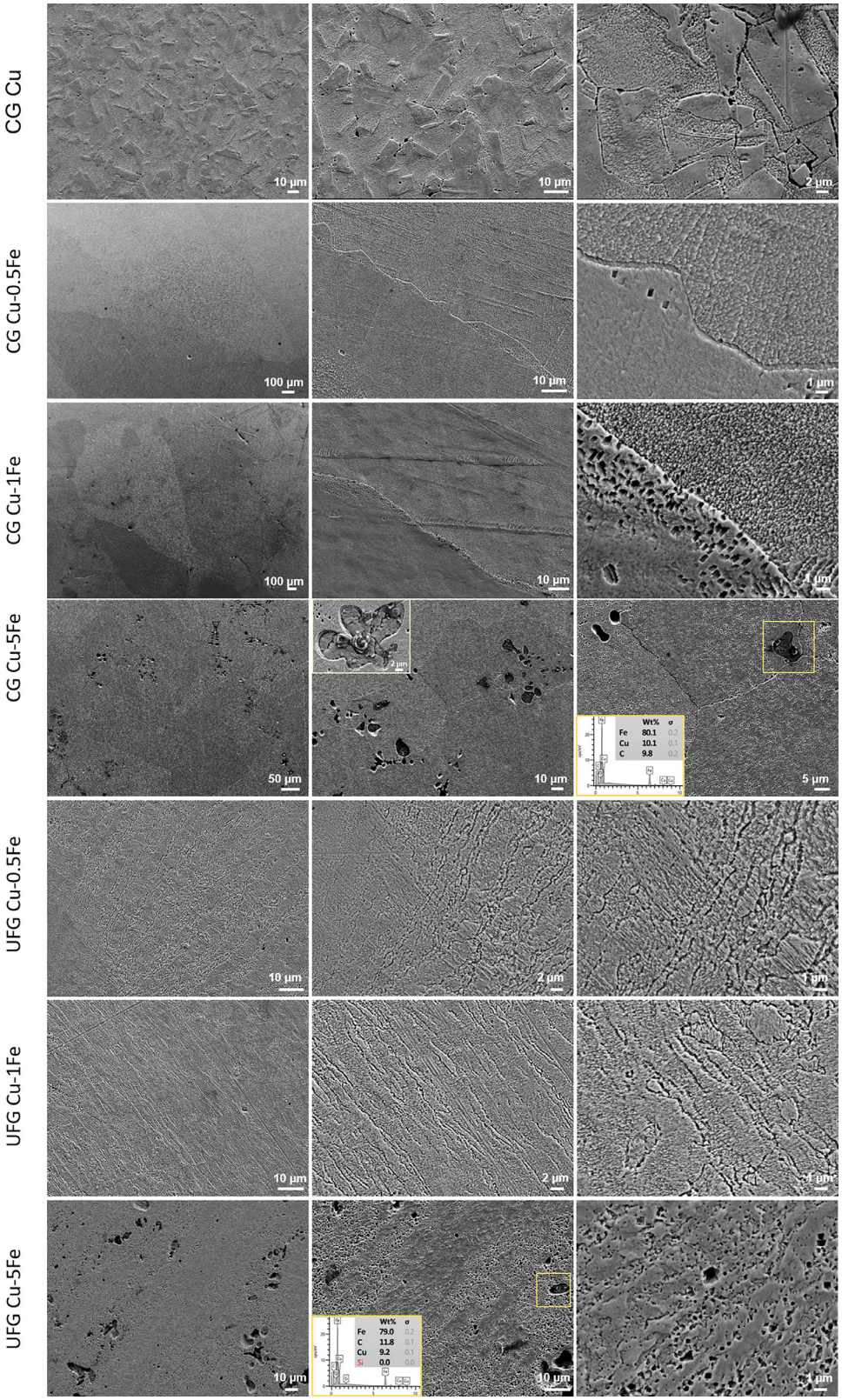

Fig. 1. Microstructure images of the CG Cu and CG/UFG Cu–Fe alloys at different magnifications.

high early-stage Fe^{3+}release suggests the 5 % Fe effectively inhibited the Cu^{2+} release. The Fe^{3+} release rate then decreased to a stable release rate in 15 days at ~0.06 μg/day which was similar to that of the low Fe content alloys.

The pH values of the SUF after immersed with the Cu and alloys were also monitored throughout the immersion process (Fig. S2). The pH trend was similar among the CG Cu and Cu–Fe alloys between 6.9 and 7.8, while the pH values of the SUF

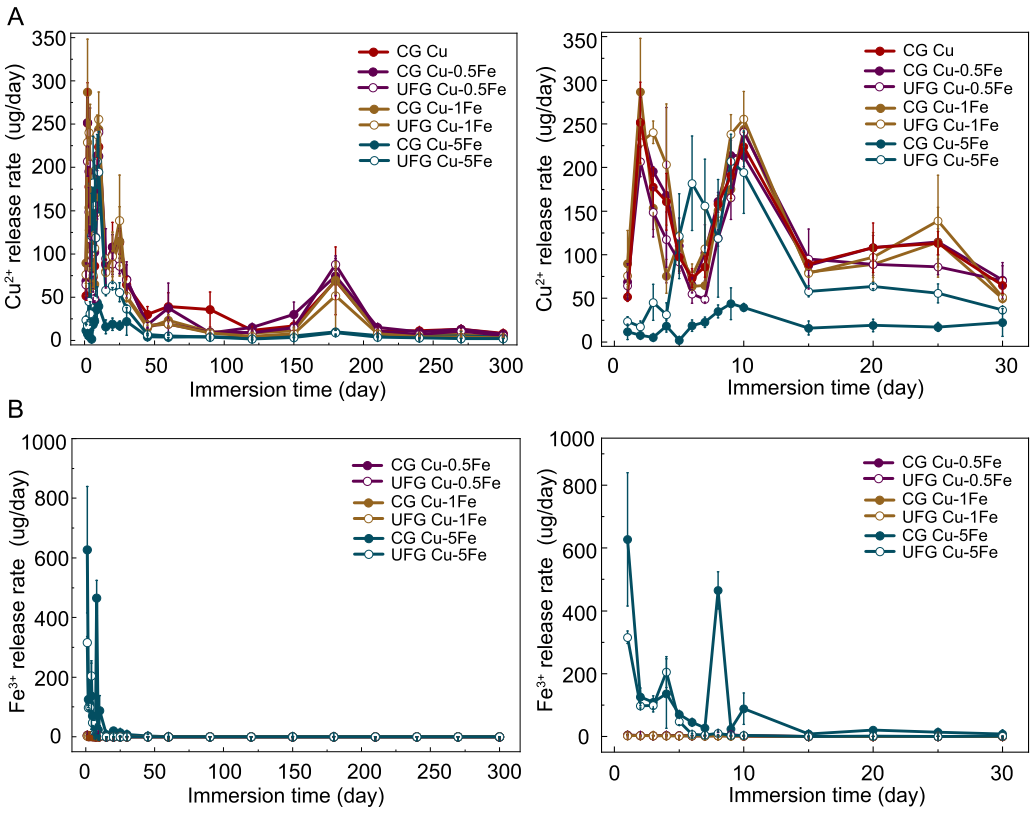

Fig. 2. The release rates of the Cu^{2+} (A, B) and Fe^{3+} (C, D) in SUF from the CG Cu and CG/UFG Cu–Fe alloys for 300 days.

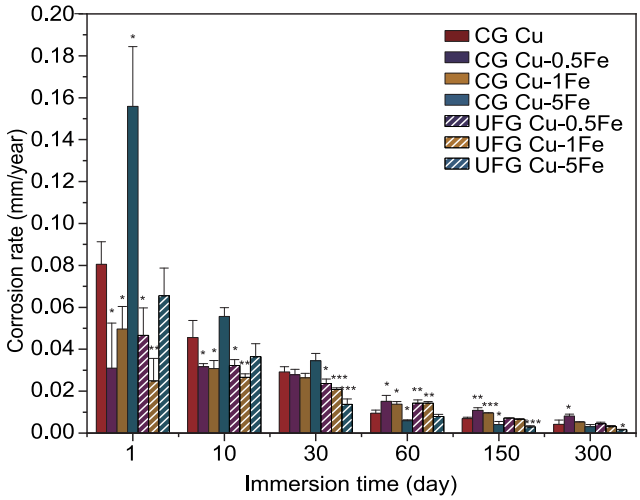

Fig. 3. The corrosion rates of the CG Cu and CG/UFG Cu–Fe alloys in SUF for 300 days.

with Cu–Fe alloys were slightly higher than that of the SUF with CG Cu.

3.3. Corrosion rates

Fig. 3 illustrates the corrosion rates of both the CG Cu and Cu-Fe alloys in SUF over a span of 300 days. Overall, the corrosion rates of all materials exhibited a gradual decrease with the prolonged immersion time. This decline can be attributed to the accumulation of corrosion products on the material surfaces, impeding direct exposure to SUF. This corrosion rate trend aligns with the ion release profiles observed in Fig. 2 for the CG Cu and the CG/UFG Cu–Fe alloys. Initially, the CG Cu–5Fe alloy demonstrated a significantly higher corrosion rate compared to CG Cu and all other alloys, particularly within the first 30 days, attributing to the release of Fe^{3+}(627.3 μg/day on the first day). However, beyond 30 days of immersion, as corrosion rates decreased for all materials, the corrosion rate of CG Cu-5Fe became lower than all others. The corrosion rate of UFG Cu–5Fe consistently remained lower than that of CG Cu due to its ultrafine grain structure and higher Fe content.

The corrosion rates of the CG/UFG Cu–0.5Fe, and the CG/UFG Cu–1Fe alloys were lower than that of the CG Cu in the first 30 days and the opposite trend was exhibited from 60 to 300 days, suggesting the suppressed burst release in the beginning and well-maintained high release in long-term immersion for the Cu–Fe alloys.

3.4. Characterization of corrosion morphology and products

Figs. 4 and S3 show the surface corrosion morphology and corrosion product composition of the CG Cu and the Cu–Fe alloys after the immersion in SUF for 1, 10, 30, 60, 150, and 300 days. It can be seen clearly from Fig. 4 that there were more accumulated corrosion products on the surface for all the materials with the longer immersion time and the components of the corrosion products increased as well (Fig. S3). Consistent with the ion release results, the evolution of the corrosion morphology and composition exhibited two distinct patterns. The Cu alloys containing low Fe content (CG/UFG Cu–0.5Fe/1Fe) presented similar corrosion morphology and composition progress to the CG Cu. The corrosion products of the CG Cu and Cu–0.5/1Fe alloys were in the form of particles covering the surface along the grinding groves as a thin single layer. With the prolonged immersion time, the thickness and density of corrosion product layer gradually increased in 30 days. The main corrosion product was Cu_2O on the surfaces within 60 days' immersion (Fig. S3). The corrosion products started to ac-

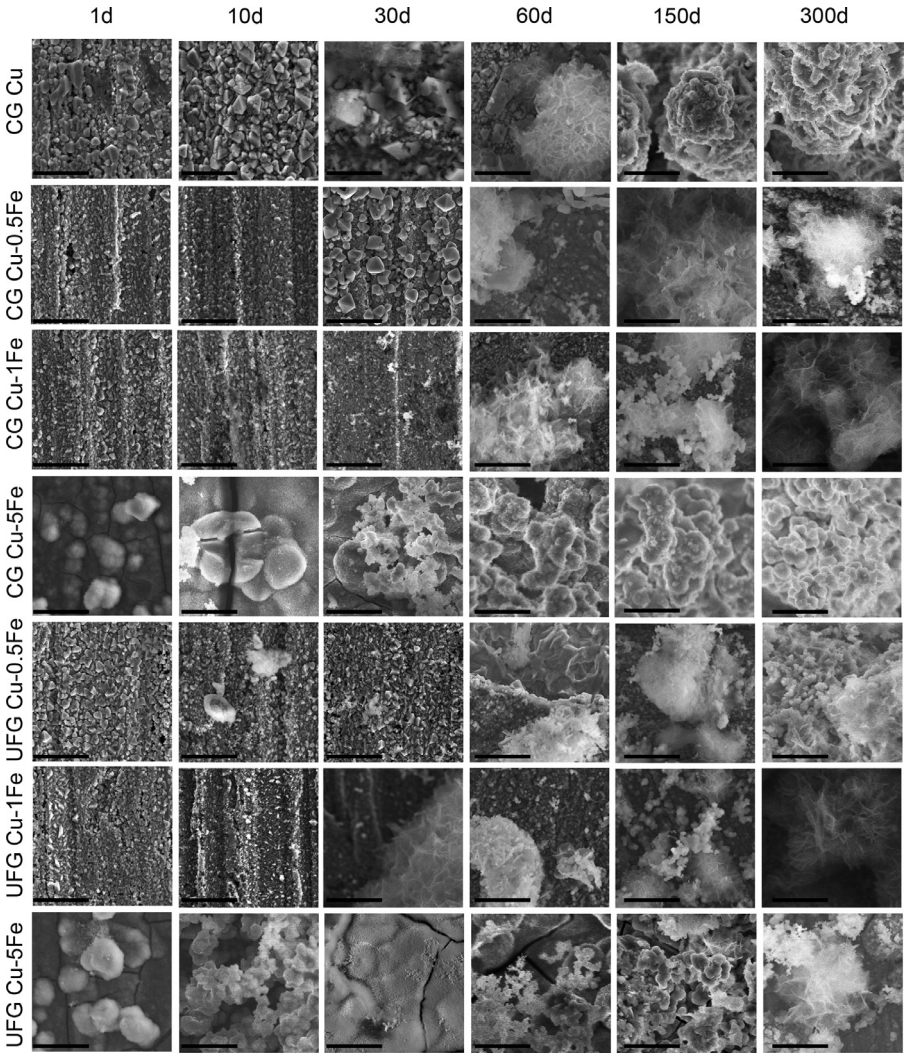

Fig. 4. Surface corrosion morphology of the CG Cu and CG/UFG Cu–Fe alloys after the immersion in SUF for 1, 10, 30, 60, 150, and 300 days. The scale bars in the SEM images were 5 μm.

cumulate into three-dimensional flower-shaped particles, forming loose but thick layers from 150 to 300 days. However, the main corrosion product was still Cu_2O with increased amount. KCl was detected from the corrosion products of CG/UFG Cu–0.5/1Fe for 150- and 300-days' immersion. It could be the deposition of the salt from SUF. On the other hand, the CG/UFG Cu-5Fe alloys displayed bumpy surfaces with non-uniform large particles within 1 day's immersion already. Thick corrosion product layers formed in 10 days with larger porous particles in flower shape and kept increasing the density and thickness of the corrosion product layers from 30 days to 300 days. The detected corrosion product was also only Cu_2O. A small peak at 44.6 ° was presented in the XRD spectra of only the CG/UFG Cu-5Fe alloys, attributing to the signature peak of Fe, suggesting the Fe phase in the alloy and the different corrosion morphology might be attributed the corrosion products related to Fe phase.

The EDX spectra in Fig. S4 exhibited the elemental compositions of the corrosion products of all the materials immersed for 1 day and 300 days. It can be observed that on the first day of immersion, Cu and O were detected in the corrosion products of all materials, but the additional Fe, P, Ca, and C were detected on the surfaces of CG/UFG Cu-5Fe, which could correspond to the amorphous spheres. Table S1 listed the quantitative analysis of the elements in the corrosion surface of the CG Cu and all Cu alloys. The weight percent of Cu on the surfaces of CG/UFG Cu–5Fe (4.9 wt%, & 4.7 wt%) were much lower than that of the CG Cu and low Fe content Cu alloys. This also suggested the Fe predominated corrosion of CG/UFG Cu–5Fe in early immersion period. By the 300th day of immersion, Cu, O, P, Cl and Ca were detected on the surfaces of both the CG Cu and low Fe content Cu alloys, while Fe was presented for high Fe content in CG/UFG Cu-Fe alloys.

3.5. Electrochemical analysis of the CG Cu and CG/UFG Cu–Fe alloys in SUF

Since the CG/UFG Cu–0.5Fe and CG/UFG Cu–1Fe alloys exhibited very similar corrosion properties and Cu^{2+} release with the CG Cu, we focused on the comparison of the CG/UFG Cu–5Fe alloys and the CG Cu in the electrochemical tests. Fig. 5A showed the polarization curves of the CG Cu, CG Cu–5Fe, and UFG Cu–5Fe in SUF. The similar polarization plots of the three materials exhibited passive-like dissolution behaviors in SUF [36]. The corrosion current density followed the order: CG Cu > CG Cu-5Fe > UFG Cu–5Fe, respectively. Fig. 5B showed the Tafel slopes of the selected region of the polarization plots of CG Cu, and CG/UFG Cu–5Fe in Fig. 5A. The slopes calculated in Fig. 5B descended in the order of CG Cu > CG Cu–5Fe > UFG Cu–5Fe.

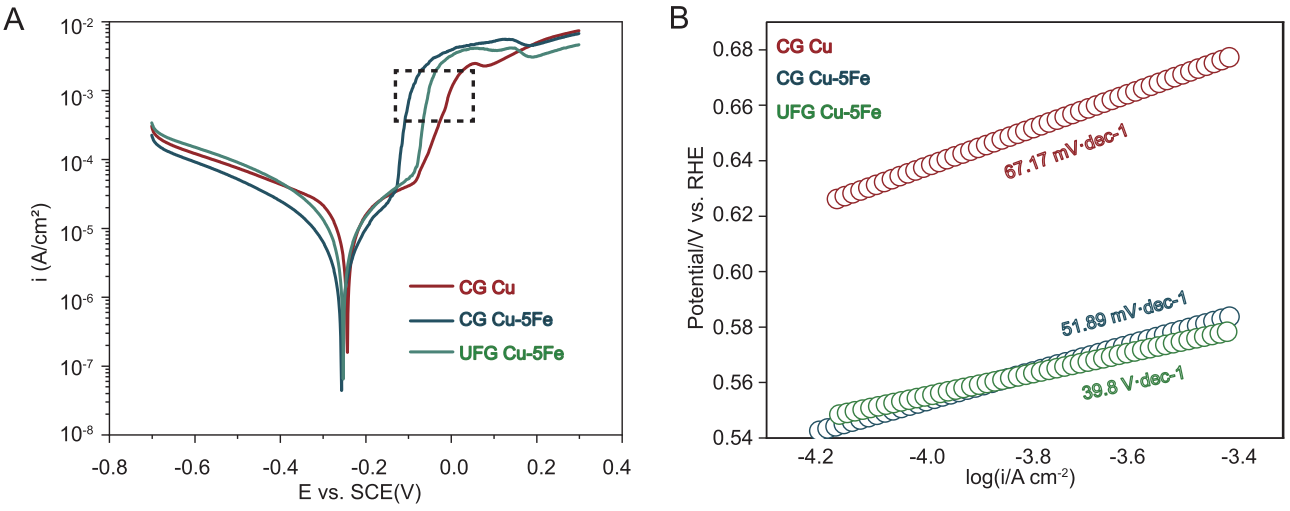

Fig. 5. The electrochemical polarization curves (A) and the Tafel slops (B) of the CG Cu, CG Cu-5Fe, and UFG Cu–5Fe alloys in SUF.

The polarization and the Tafel results suggested that the CG/UFG Cu–5Fe alloys were more easily corroded than the CG Cu before corrosion equilibrium was reached in SUF, but it turned more difficult for these two alloys to corrode after equilibrium was reached. It could be deduced from both ion release results in Fig. 2 and the electrochemical results that the corrosion occurred to Fe first in the Cu–5Fe alloys owing to the galvanic corrosion as Fe is more electrochemically active than Cu, so that the CG/UFG Cu–5Fe alloys more easily corroded than the CG Cu. Moreover, the Cu–5Fe alloys showed the inhibited burst release of Cu^{2+}. The corrosion rates of both the alloys was reduced after equilibrium with a passivation film quickly formed on the surface of the alloys.

3.6. Cytotoxicity assay

Figs. 6 and S5 exhibit the results of the cytotoxicity evaluation on the CG Cu and all Cu–Fe alloys. It can be observed that the viabilities of all the cells of HEEC, HESC and HUVEC treated with 100 % (Fig. 6A, C, &E) and 50 % (Fig. S5) extracts of the CG Cu, Cu–0.5Fe and Cu–1Fe alloys were within the range of 3.5–30.2 % which is significantly lower than the negative control group and even lower than the positive control group (treated with 10 % DMSO). The low cell viability was consistent across the 1, 2, and 3 days, indicating severe cytotoxicity of the CG Cu, Cu–0.5Fe and Cu–1Fe alloys towards all the cell lines. There was no significant difference in the cell viability between the CG and UFG structured alloys of Cu–0.5Fe and Cu–1Fe, suggesting that the grain size reduction within the two low Fe containing Cu alloys did not affect biocompatibility noticeably. However, it is worth noting that the high Fe containing Cu alloy, Cu–5Fe in both coarse and ultra-fine grains, displayed dramatically high cell viability of all three cell lines. The cell viability of the HEEC treated with 100 % exact of CG Cu–5Fe alloy was 90.7 % in the first day and then decreased to 35.8 % and 17.7 % in the day 2 and 3. On the contrary, the viability of the HEEC treated with 100 % UFG Cu-5Fe exact presented increased trend with the culture time from 56.1 % to 79.2 %. For the cell line of HESC, the viability after treated with 100 % exacts of CG Cu–5Fe alloy shows extraordinarily high (88.3–121.0 %) through 3 days. The viability of the HESC treated with 100 % UFG Cu–5Fe alloy exact was also very consistent through the 3 days (~80 %). For the cell line of HUVEC, the effect of the 100 % extract of CG Cu–5Fe alloy to the viability was relatively obvious, the viability ranging from 50.4 % to 14. 3 % in day 1 to 3. On the other hand, the cell compatibility UFG Cu-5Fe alloy to the HUVEC was very high with the viability values of 72.7–112.5 %, especially in day 2 and 3.

Fig. 6B, D, &F present the cell viabilities of the HESC, HEEC and HUVEC treated with 10 % alloy extracts of the CG Cu and Cu–Fe alloys. It can be seen that all the cell viability with the diluted alloys extracts were greatly increased. In generally comparison, the CG/UFG Cu–0.5Fe and Cu–1Fe presented similar or slightly higher cell compatibility than the CG Cu, while the Cu–5Fe alloys in both CG and UFG microstructures exhibited higher viability of all three cell lines than CG Cu. It is also can be found that the viability of the cell lines treated with the of UFG Cu–5Fe alloy exacts in all concentrations (100 %, 50 % and 10 %) were consistently high.

Overall, the *in vitro* cytotoxicity experiments display that the CG Cu–5Fe and UFG Cu–5Fe exhibit much enhanced cell biocompatibility, which might be attributed to the reduced Cu^{2+} from the alloying Fe and further owing to the ultrafine grained structure.

3.7. Transcriptomic analysis

To further explore the different cell response of the CG Cu and CG Cu-–5Fe alloy, the transcriptomic analysis using the cell line of HESC was carried out. The experimental group cells were treated with the 50 % extracts of the CG Cu, and CG Cu–5Fe for 12 h. The cell morphology was observed and shown in Fig. 7A. It can be seen that there was no observable difference in the cell morphology for the CG Cu–5Fe alloy compared to the control group, whereas the cell edges of the HESC cultured in the extract of the CG Cu presented brightened wrinkles and the cells tended to round up, indicating that the HESC cells had been subjected to toxicity environment.

Fig. 7B shows the principal component analysis among the three groups, from which it can be observed that the CG Cu group can be significantly distinguished from both the NC group and CG Cu–5Fe. Fig. 7C showed the Wayne diagram results of the three groups of genes, with 9520 common genes in the three groups. In addition, there were1043 common genes presented only in the NC group and CG Cu–5Fe group, which was significantly higher than the number of common genes only presented in both the NC and CG Cu group (21) or only presented in both the CG Cu and CG Cu–5Fe group (160). The results illustrated that the CG Cu–5Fe group had higher similarity to NC group. Furthermore, the expression levels of genes in the three groups were compared among the three groups (Fig. 7D). The quantitative analysis in Fig. 7E shows that the CG-Cu group displayed significant differences compared to the control and CG Cu-5Fe groups, and the greatly higher number of gene expression were 4280 and 1033. Statistical analysis of

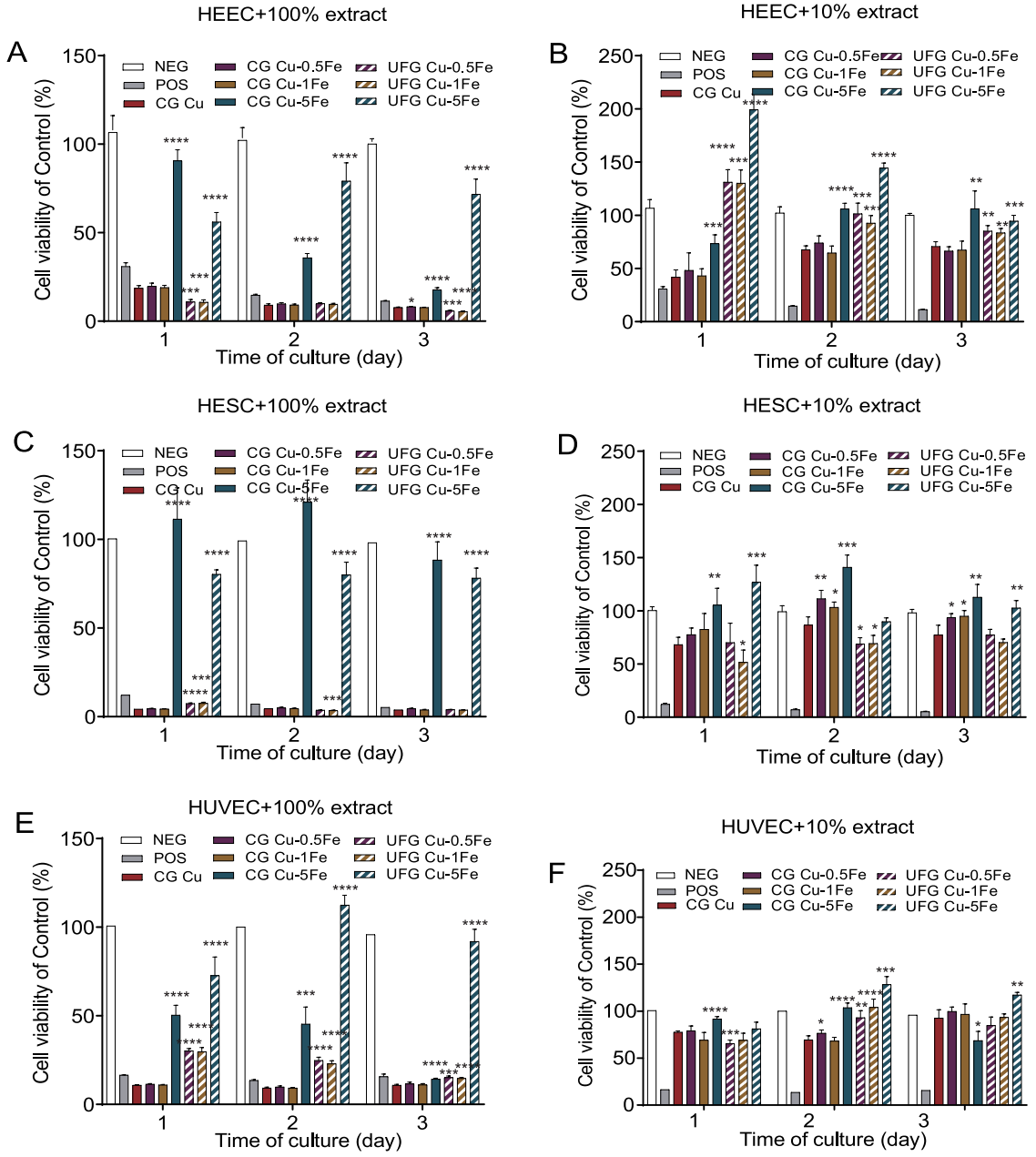

Fig. 6. The cell viabilities of the HEEC (A and B), HESC (C and D), and HUVEC (E, F) treated with 100 % and 10 % extracts of the CG Cu and CG/UFG Cu-Fe alloys for 1, 2, and 3 days. $^{***}P \leq 0.0001$, $^{***}P \leq 0.001$, $^{**}P \leq 0.01$ and $^{*}P \leq 0.05$ when the cell viability of the Cu–Fe alloys extracts compared with that of the CG Cu extracts.

these two situations were carried out and showed in Fig. 7F& G. The P-values were 3.1e-08 and 0 for the profile #2 and #5, respectively, indicating significant differences. Fig. 7H& I shows the GO enrichment analysis and it can be seen that significantly highly expressed genes in the CG Cu group were mainly involved in cell death, cell death regulation, apoptosis regulation, and negative regulation of cellular and biological processes. On the contrary, genes with significantly low expression in the CG Cu group were mainly involved in DNA repair, various biological processes, and synthesis and metabolism of various molecules (Fig. 7I). These results indicate that high concentration of Cu^{2+} can deactivate cell survival processes such as intracellular biosynthesis, and would promote cell apoptosis and cell death. In the CG Cu–5Fe group, the release of iron inhibited the release of copper, and the concentration of copper ion was significantly reduced, which protected the cells from the damage caused by high concentration of Cu^{2+}.

3.8. The Cu^{2+} and Fe^{3+} concentrations in the extracts and pH values

The concentrations of the Cu^{2+} and Fe^{3+}in the extracts of the CG Cu and Cu-Fe alloys were measured in the in the DMEM/F12 complete medium for HEEC/HESC and ECM complete medium for HUVEC using ICP-MS and the results are listed in Table 1. In both mediums, the original concentration of Cu^{2+} and Fe^{3+} were very low, 0.021–0.025 μg/mL and 0.271–0.304 μg/mL. In the DMEM/F12, the CG Cu, CG/UFG Cu-0.5/1Fe alloys released the Cu^{2+} and Fe^{3+} in the ranges of 153–196 μg/mL and 0.58–1.3 μg/mL, respectively. While in the ECM, the concentrations of the released Cu^{2+} were similar, around 93.4 μg/mL, and Fe^{3+} was at roughly 0.25 μg/mL. There was no significant difference in either Cu^{2+} or Fe^{3+} released from the CG Cu and CG/UFG Cu–0.5/1Fe. However, the Cu^{2+} concentrations in the CG Cu–5Fe and UFG Cu–5Fe extracts were significantly decreased to 14 μg/mL and 1.6 μg/mL within DMEM/F12,

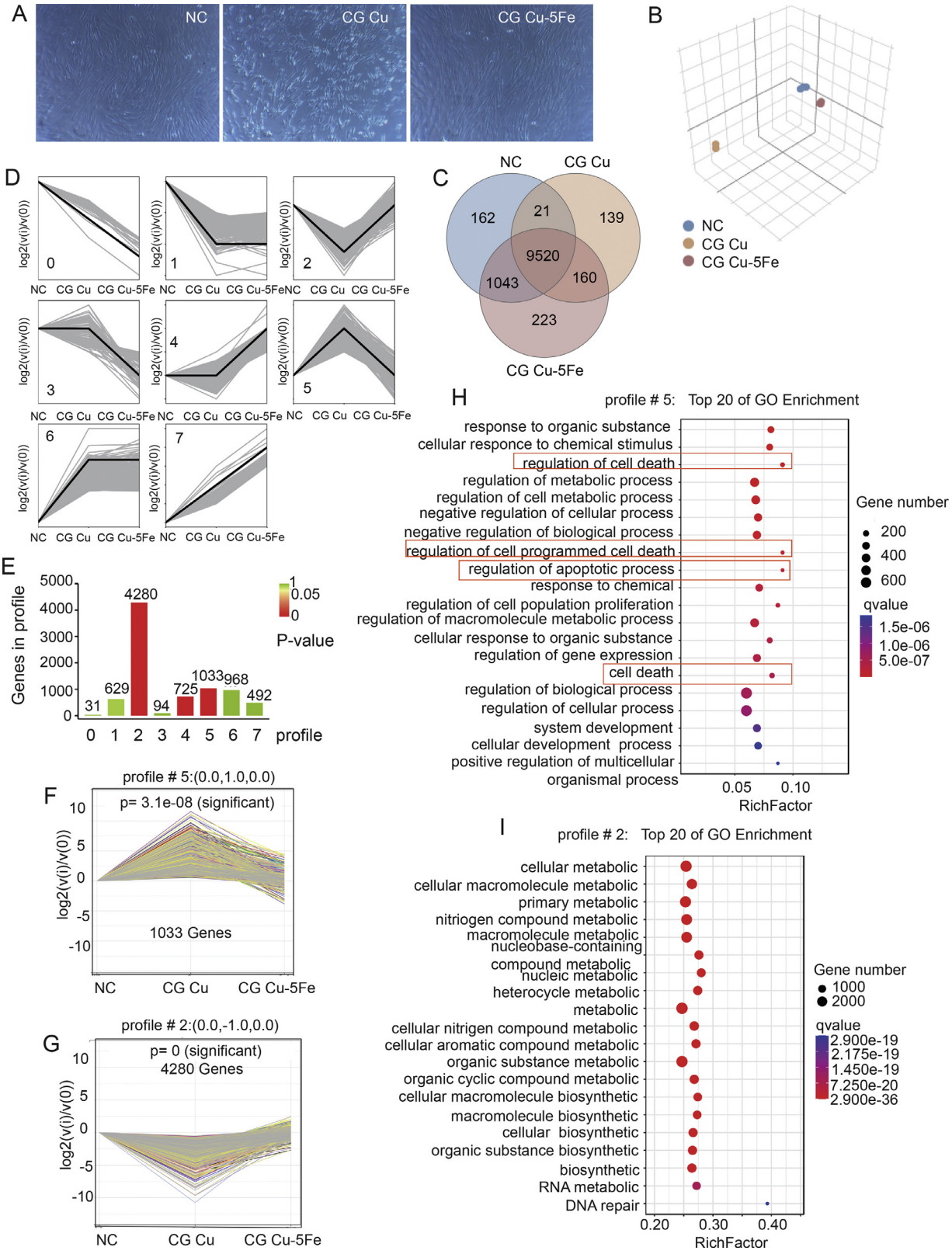

Fig. 7. (A) Cell morphology of HESC after treated with the 50 % extracts of the CG Cu and CG Cu-5Fe for 12 h, respectively; (B) The principal component analysis (PCA); (c) Venn diagrams and (D) comparison of gene expression levels of genes in the three groups; (E-G) The number of genes in different profiles; (H, I) GO enrichment analysis of significantly high or low expression genes in the CG-Cu group.

Table 1
The Cu^{2+} and Fe^{3+} concentrations in the cell medium extracts of the CG Cu and Cu–Fe alloys.

	DMEM/F12 for HEEC/HESC		ECM for HUVEC	
	Cu^{2+} (μg/mL)	Fe^{3+} (μg/mL)	Cu^{2+} (μg/mL)	Fe^{3+} (μg/mL)
NC	0.0210 ± 0.0004	0.304 ± 0.008	0.0250 ± 0.0005	0.271 ± 0.004
CG Cu	192 ± 15	0.150 ± 0.004	93 ± 6	0.119 ± 0.007
CG Cu–0.5Fe	159 ± 12	0.58 ± 0.03	91 ± 3	0.231 ± 0.004
CG Cu–1Fe	153 ± 8	1.3 ± 0.3	92 ± 4	0.248 ± 0.009
CG Cu–5Fe	**14 ± 11***	**48 ± 24#**	**18 ± 12***	**54 ± 13###**
UFG Cu–0.5Fe	194 ± 8	0.54 ± 0.02	102 ± 2	0.27 ± 0.04
UFG Cu–1Fe	196 ± 17	0.53 ± 0.03	97 ± 4	0.21 ± 0.01
UFG Cu–5Fe	**1.6 ± 0.2*****	**92 ± 4###**	**1.5 ± 0.2*****	**82 ± 8###**

*$P \leq 0.05$ and ***$P \leq 0.001$ when compared with the concentration of Cu^{2+} of CG Cu group in ECM and DMEM/F12 complete medium respectively.
$P \leq 0.05$ and ### $P \leq 0.001$ when compared with the concentration of Fe^{3+} of CG Cu group in ECM and DMEM/F12 complete medium respectively.

Table 2
Antifertility evaluation of the CG Cu, CG Cu–5Fe alloy, and UFG Cu–5Fe alloy.

Group	Number of rats	Number of embryos in the uterine horn		Number of pregnant rats	Antifertility rate (%)
		with rod specimen	without rod specimen		
NC	10	7.9 ± 1.7	7.9 ± 1.3	10	0
Sham	10	7.7 ± 1.0	7.8 ± 1.2	10	0
CG Cu	20	0	7.8 ± 1.3	0	100
CG Cu–5Fe	20	0	7.9 ± 1.5	0	100
UFG Cu–5Fe	20	0	7.9 ± 1.9	0	100

and 18 μg/mL and 1.5 μg/mL within ECM. Meanwhile, Fe^{3+} concentrations much increased to 48 μg/mL and 92 μg/mL in DMEM/F12 and 54 μg/mL and 82 μg/mL in ECM, respectively.

The pH values of the extracts within both mediums in Fig. S6 were very close without significant difference among the CG Cu and CG/UFG Cu–Fe alloys.

3.9. In vivo *antifertility tests*

The contraceptive effectiveness of the CG Cu, CG Cu–5Fe alloy, and UFG Cu–5Fe alloy was evaluated by implanting the rod specimen into the rats' right-side uterine horn for 28 days. The results are summarized in Table 2. In the control and sham surgery groups, 8 embryos on average were found in each side of uterine and all rats were pregnant. In the group of rats with the implantations, no embryo was observed in the right-side uterine bearing the CG Cu or CG/UFG Cu–5Fe rods, while 8 embryos on average were found in the contralateral uterine without the rod implants. Despite of the formation of embryos in one uterine horn, there was no pregnancy found in the rats. The contraceptive rate for all Cu and Cu–5Fe alloys was 100 %. The same embryos number in the contralateral uterine exhibited no statistically significant difference among the three materials, suggesting that the addition of 5 % Fe to the Cu did not affect the contraceptive effectiveness within the 28 days of contraceptive experiments.

3.10. *Histological observation*

Fig. 8 shows the tissue morphology of the rats' uterine cavity in the control group and in the rats bearing CG Cu and CG/UFG Cu–5Fe alloys implants at the time points of 3 days, 7 days, 14 days and 28 days. It can be observed that, at each time point, the uterine cavity tissues of the rats in the control group remained intact, the epithelial cell layer was complete, and no sign of inflammation was found. While on the 3rd day of the CG Cu implantation, the rat's uterine already exhibited significant tissue damage and severe acute inflammatory reactions were induced. The uterine cavity was narrow, neither epithelial cells nor glands were present on the top surface. A substantial infiltration of inflammatory cells was observed (pointed using red arrows). On the 3rd day of the CG Cu–5Fe alloy implantation, the epithelial cell layer of the uterine cavity was partially lost with a relatively small area infiltration of inflammatory cells. The inflammatory symptoms were not significant. On the same time point of the UFG Cu–5Fe alloy implantation, the rat's uterine tissue presented a mostly intact epithelial cell layer with only a much smaller amount of inflammatory cell infiltration, suggesting the mildest inflammation. Further observation on the 7th day implantation, the inflammatory reactions in the uteri of the rats bearing the CG Cu, CG Cu–5Fe, and UFG Cu–5Fe alloy implants all were intensified compared to that on the 3rd day. In the uterine cavity bearing with the CG Cu, many inflammatory cells had spread into the uterine muscle layer, accompanied with a few neutrophils (black arrows). With the CG Cu–5Fe or UFG Cu–5Fe alloy, the inflammation of the uterine cavity was still mild with a small number of neutrophils presenting in the uterine cavity with the UFG Cu–5Fe.

After 14 days of implantation, the inflammatory reaction in the uterine cavity implanted with the CG Cu further intensified, while the uterine cavity with the CG Cu–5Fe alloy exhibited the phase of recovery. The epithelial cell layer became intact, and a small number of inflammatory cells, very few neutrophils in the uterine muscle layer, and no inflammatory exudate were presented. With the UFG Cu–5Fe group, the uterine cavity displayed partially intact epithelial cell layer, a few of inflammatory cells, and a small number of neutrophils in the uterine tissue. By the 28th day of the implantation, the symptoms of inflammatory damage in the uterine cavity with the implanted materials were all significantly reduced although a few neutrophils could be found in the uterine tissue. In the CG Cu implanted uterine cavity, inflammatory cells decreased and the epithelial cell layer was gradually formed. While in the CG Cu–5Fe or UFG Cu–5Fe implanted uterine cavity, the uterine tissues had almost fully recovered to the condition of control group. At each time point, the extent of uterine tissue damage in the groups of CG/UFG Cu–5Fe was lower than that in the CG Cu group. This suggests that 5 % Fe alloyed with Cu can significantly improve the histocompatibility of Cu-containing materials as

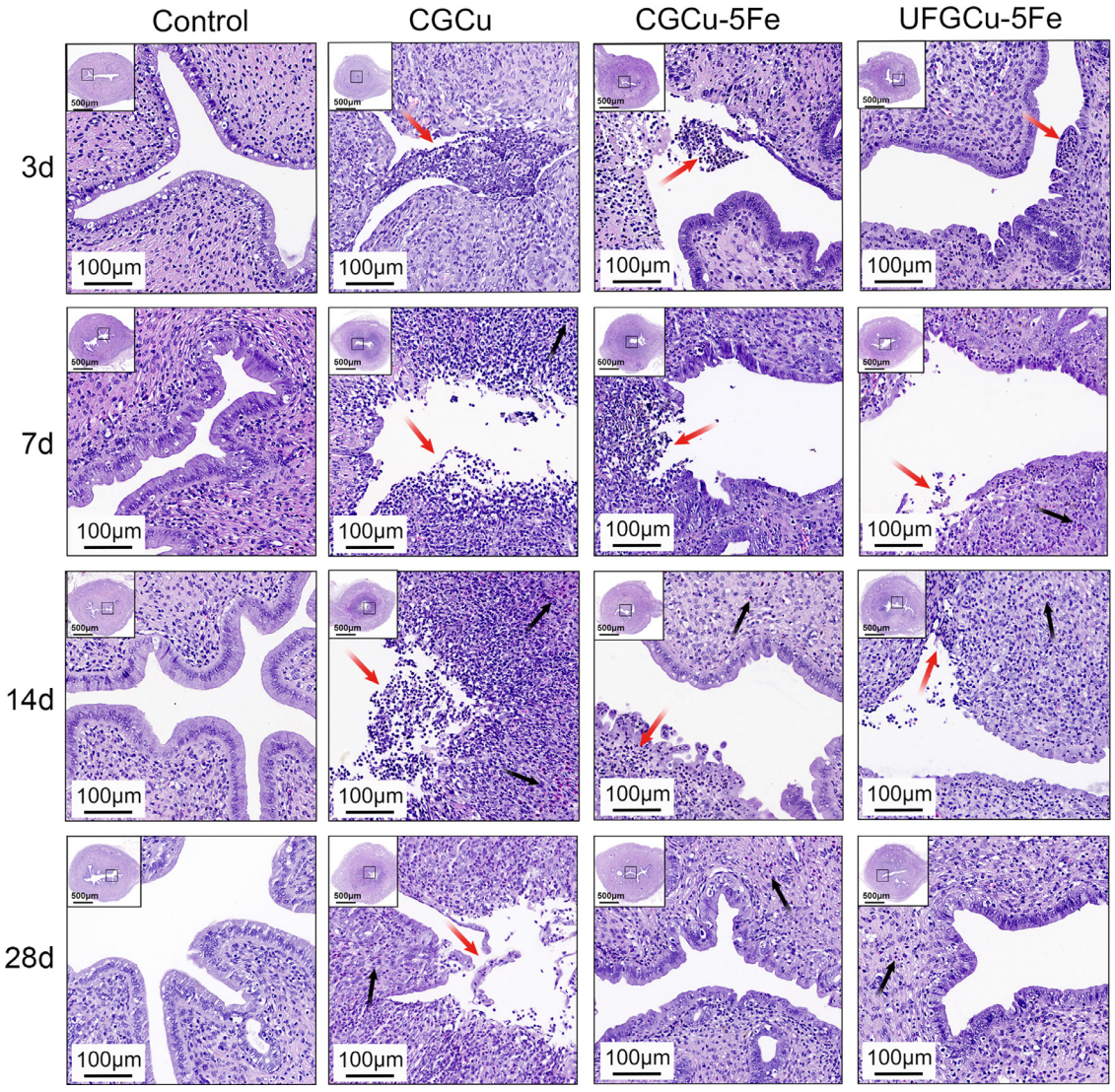

Fig. 8. Histopathology images of the endometrium of the rat uterine cavity implanted with the CG Cu, CG Cu–5Fe, and UFG Cu–5Fe rods for 3 days, 7 days, 14 days and 28 days. Red arrow indicates inflammatory cells, and black arrow points to neutrophils.

the active material of Cu-IUD, reduce the degree of inflammatory reaction at the implantation site, and at the same time promote the repair of inflammation-induced tissue damage.

3.11. *Characterizations of the* in vivo *implanted materials*

The corrosion morphology of the CG Cu, CG Cu–5Fe and UFG Cu–5Fe rods after implanted in the rat uterine for 3 days, 7 days, 14 days and 28 days was shown in Fig. 9. It can be seen that with the prolonged implantation time, there were more corrosion products formed on the surface of the rods. Multiple layers of corrosion products were found from 14 days and products on the surface could peel off from 14 to 28 days for CG Cu and CG Cu–5Fe rods. The UFG Cu–5Fe rod exhibited much more uniform corrosion products on the rod surface without much peelings, suggesting the uniform surface corrosion of UFG Cu–5Fe owing to the ultrafine grained structure.

XPS for composition analysis was performed on the rod surfaces of the CG Cu, CG Cu–5Fe, and UFG Cu–5Fe alloys after implantation for different time points. The XPS survey spectra are shown in Fig. S7. It can be observed that the elements on the superficial surface of the CG Cu contained Cu, O, Ca, C and N for all the implanted time durations (3, 7, 14, and 28 days). Other than aforehand elements, on the surfaces of the CG Cu–5Fe and UFG Cu-5Fe alloys, the element of Fe was shown for both 3 and 7 days of implantation. However, Fe element was not observable in the survey spectra for the Cu–5Fe alloys after the implantation for 14 and 28 days. It might be because the thicker corrosion products were accumulated on the surface too much to detect Fe.

Fig. 10 displays the XPS region spectra of Cu $2p_{3/2}$ (from 929 eV to 947 eV) and the region spectra of Fe $2p_{3/2}$ (from 705 eV to 720 eV) of the corrosion products on the surfaces of the three materials after implanted for 3, 7, 14, and 28 days. Two valences of Cu, specifically Cu^{+} and Cu^{2+}, were found from the fitted analysis on the Cu region spectra of Cu $2p_{3/2}$ (Fig. 10A–D). The binding energy of Cu^{2+} at 934.4 eV in $Cu(OH)_2$, 933.8 eV in CuO, and 934.5 eV in $Cu_2(OH)_2CO_3$ were all found [37]. The binding energy of Cu^{+} at 932.5 eV in Cu_2O, and 931.9 eV in CuCl [38] was observed as well, demonstrating the corrosion product on the surface containing possible compounds like these. The binding energy of zero valence Cu metal is around 932.5 ± 0.2 eV [39,40] which is too close to that of Cu_2O to be distinguished using the region spectra of Cu $2p_{3/2}$. The Kinetic Energy of Cu LMM Auger peak of Cu_2O at 916.8 eV and the peak of Cu metal at 918.6 eV confirmed

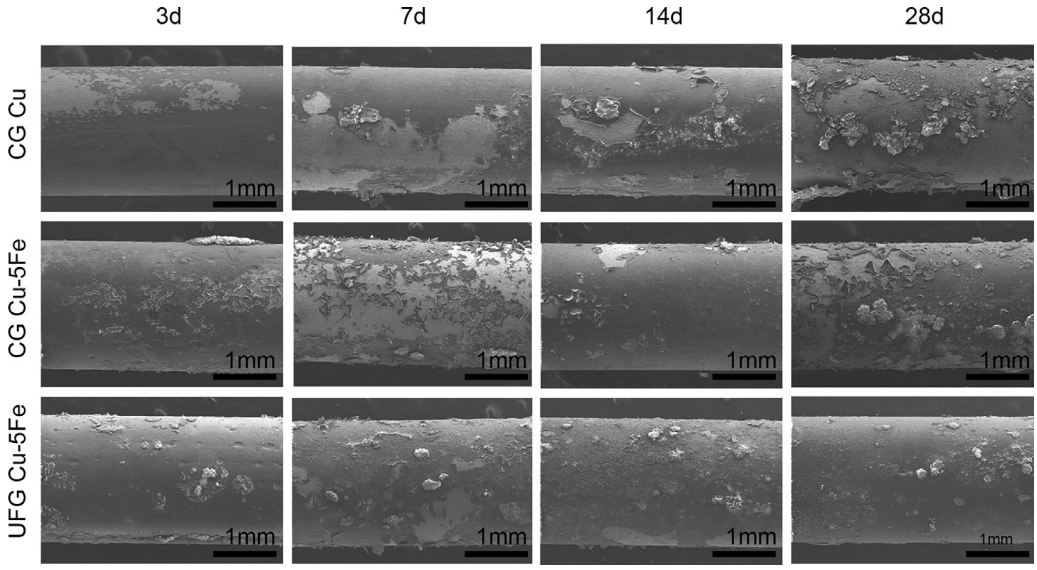

Fig. 9. Corrosion morphology of the CG Cu, CG Cu–5Fe, and UFG Cu–5Fe after implanted in rats' uterus for 3, 7, 14 and 28 days.

the presence of Cu (Fig. S7). With the prolonged implantation time, the detected compounds on the Cu and Cu–5Fe alloys were similar, containing both Cu, Cu^{+} and Cu^{2+} compounds.

Fig. 10E–H display the XPS region spectra of Fe $2p_{3/2}$ within the range of 710–715 eV. From both the region spectra of the CG Cu–5Fe and UFG Cu–5Fe alloy for all the time duration, the compound of Fe_2O_3 with the binding energy at 710.8 eV and other states of Fe^{3+} were observed in the corrosion layers after 3, 7, 14, and 28 days. Furthermore, CG Cu–5Fe showed FeO with the binding energy at 708.4 eV [41] in the corrosion product. At 28 days, $Fe(OH)_3$ with the binding energy at 711.5 eV was also presented. UFG Cu–5Fe exhibited the similar corrosion components to the CG Cu–5Fe, however, the additional component, such as FeO, appeared in a relatively late stage. The $Fe(OH)_3$ was not found in 28 days corrosion product for the UFG Cu–5Fe alloy.

The EDX analysis of the corrosion products on the CG Cu and CG Cu–5Fe and UFG Cu–5Fe alloys was carried out and the results were shown in Table S2. The main metallic elements found in the corrosion products on the material surfaces were Cu, Fe and Ca and non-metallic elements were C, O, P, S and N. The presence of Fe was found only in the Cu–5Fe alloys. The P might be attributed to the uterus fluid while the S and N might be attributed to the attachment of protein or other biological molecules in the uterine. The EDX results are consistent with the XPS analysis.

Fig. S8 displays the XRD analysis on the phase composition of the corrosion product of the implanted CG Cu, CG Cu–5Fe, and UFG Cu–5Fe alloys in rats uterine for different days. It can be observed that the main corrosion products of all the three materials were Cu related compounds CuO, Cu_2O, CuCl, and Cu(OH)Cl and also the high peaks of $CaCO_3$. The Cu related compounds agreed well with the XPS analysis results.

4. Discussion

After systematic investigations in various properties of the CG Cu and CG/UFG Cu–Fe alloys, we can see that the CG Cu–5Fe is the best candidate for Cu-IUD as it is capable of significantly inhibiting the burst release of Cu^{2+}, remarkably improving biocompatibility for both *in vivo* and *in vitro* evaluations, and exceptionally effective of contraception. We did a careful analysis on the corrosion mechanism of the CG Cu–5Fe and also a through summary and comparisons on the Cu alloys as active materials for IUD.

4.1. Corrosion mechanism of the CG Cu and CG Cu–5Fe

The corrosion process of Cu in SUF has been studied previously [42,43]. When pure Cu is immersed in SUF, a porous Cu_2O layer is firstly generated, as indicated by Eqs. (1) and (2).

$$8Cu + 2H_2O + O_2 \rightarrow 4Cu_2O + 4H^+ + 4e^- \quad (1)$$

$$Cu_2O + 2H^+ \rightarrow 2Cu^{1+} + H_2O \quad (2)$$

The Cu_2O film surface can freely contact with oxygen, forming a large cathodic area. Here, Cu_2O is highly prone to oxidation into Cu^{2+} [44,45], as shown in Eqs. (3).

$$4Cu^{1+} + 2H_2O + O_2 \rightarrow 4Cu^{2+} + 4OH^- \quad (3)$$

In the small pore areas of the Cu_2O film, the entry of oxygen is restricted, leading to the formation of an anodic zone where solid Cu metal participates in the reaction.

$$Cu^{2+} + Cu_{(s)} \rightarrow 2Cu^{1+} \quad (4)$$

At this point, due to the absence of a stable protective layer on the material surface, the above process continues, leading to burst release of Cu^{2+}. As the immersion time prolongs, and with the presence of Cl^-, $HCO3^-$ in the solution, precipitates gradually formed on the material surface, forming a stable protective layer that impedes the corrosion of the material, as indicated by Eqs. (5) [46] and (6) [47].

$$Cu^{1+} + Cl^- \rightarrow CuCl \quad (5)$$

$$4CuCl + 2HCO_3^- + O_2 \rightarrow CuCO_3 \cdot Cu(OH)_2 + CO_3^{2-} + 2CuCl_2 \quad (6)$$

EDX results show the presence of second phase in CG Cu–5Fe material. Since Fe is more easily oxidized than Cu in SUF, the Fe-rich phase and Cu-rich phase would form a galvanic cell, with Fe as the anode and undergoing rapid oxidation reactions, as depicted in Eqs. (7) and then $Fe(OH)_2$ as in the following equations.

$$Fe - 2e^- \rightarrow Fe^{2+} \quad (7)$$

$$O_2 + 2H_2 + 4e^- \rightarrow 4OH^- \quad (8)$$

$$Fe^{2+} + 2OH^- \rightarrow Fe(OH)_2 \quad (9)$$

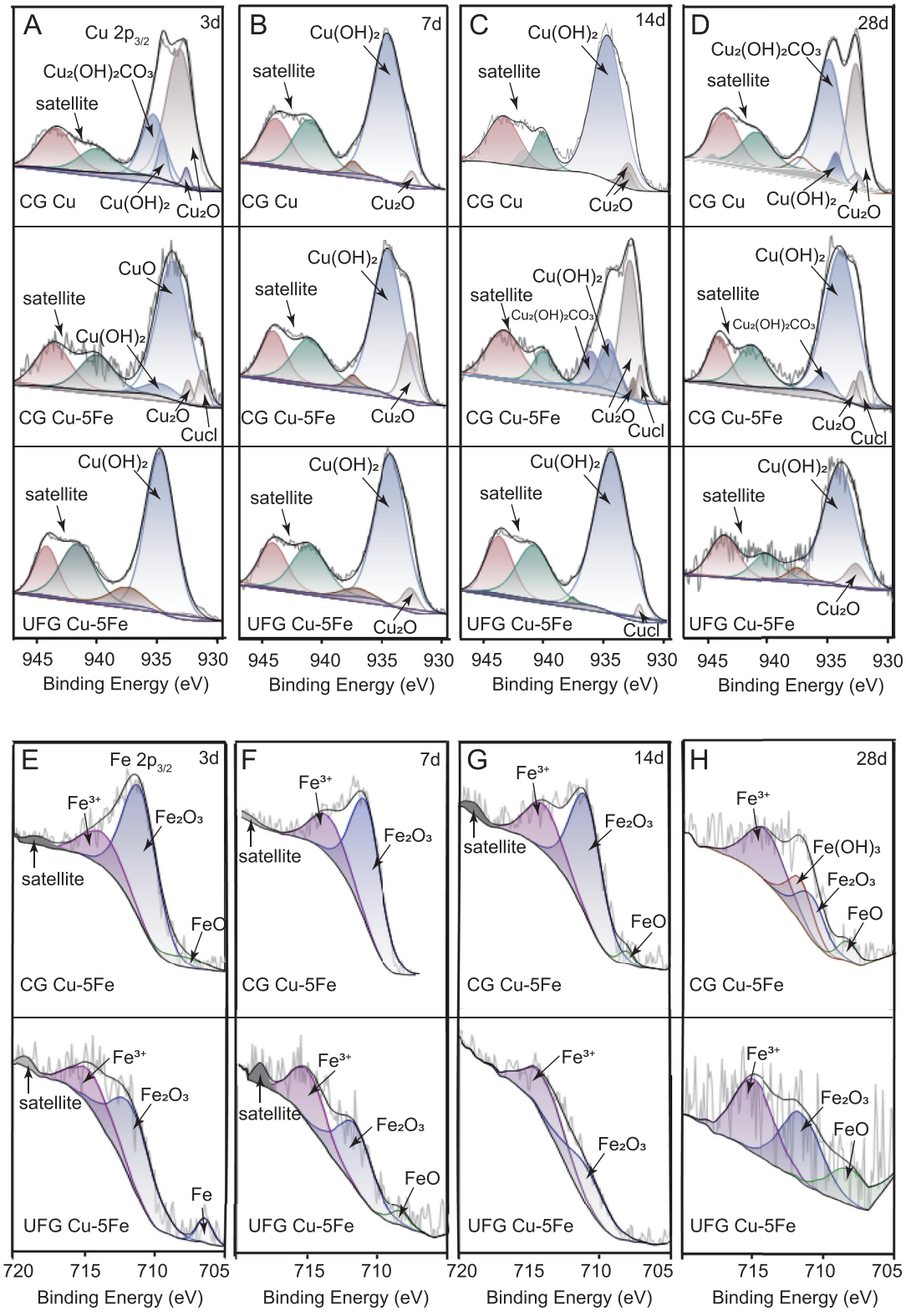

Fig. 10. The Cu2p spectra (A–D) and Fe 2p spectra (E–H) of the CG Cu, CG Cu–5Fe and UFG Cu–5Fe alloys after the implantation for 3, 7, 14, 28 days in rats' uterine cavity.

$Fe(OH)_2$ is unstable, forming a precipitate of $Fe(OH)_3$ that covers the surface of the material, as depicted in the following equation.

$$4Fe(OH)2 + O_2 + 2H_2O \rightarrow 4Fe(OH)_3 \quad (10)$$

With longer immersion time, Fe_2O_3 and FeO are generated on the surface of the alloys, as in the following equations

$$2Fe(OH)_3 \rightarrow Fe_2O_3 + 3H_2O \quad (11)$$

$$Fe + Fe_2O_3 \rightarrow 3FeO \quad (12)$$

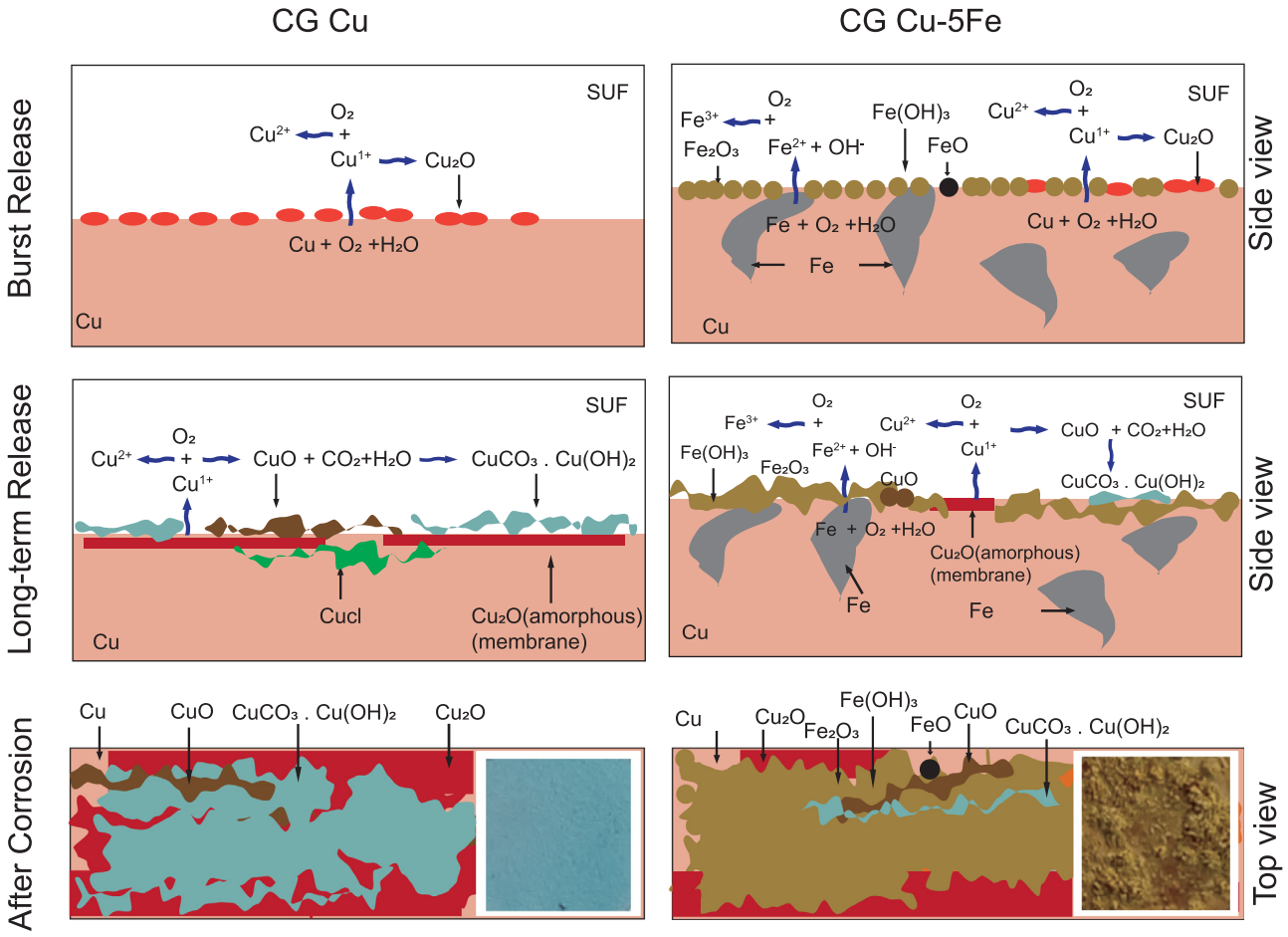

Fig. 11. Schematic illustration of the corrosion behavior of CG Cu and CG Cu–5Fe in SUF.

Due to the strong competition between the galvanic process of Fe and the pit corrosion of Cu, the precipitation of corrosion products forms a protective layer on the material surface and hinders direct contact between the alloys and SUF. The corrosion rate of Cu significantly decreases, and the release of Cu^{2+} also markedly reduces. With prolonged immersion time, the formed corrosion product layer on the alloys surface enables a minimal but steady release of ions. The corrosion mechanisms of CG Cu and CG Cu-5Fe are depicted in Fig. 11.

4.2. The summary and comparison of the Cu alloys as active materials for IUD

We summarized the properties of the CG Cu, CG Cu–5Fe and UFG Cu-5Fe in Table 3 and also compared these properties with the reported other Cu alloys and Zn alloy for the application of IUD.

The blue-shaded columns are the results from this work. By linking the grain sizes, and composition, we can see that with the addition of the 5 wt% Fe, the grain size of the CG Cu–5Fe increased to 50–250 μm. The grain size was reduced to the similar dimensions of 1–20 μm with CG Cu when the CG Cu–5Fe was processed via ECAP. The corrosion rates of the Cu and Cu alloys varied along with the grain size, the corrosion rates followed the decreasing sequence of CG Cu–5Fe, CG Cu and UFG Cu–5Fe. However, the released rate of Cu^{2+} of the CG Cu–5Fe was the lowest among the three although the released Fe^{3+} was the highest, which made up of the highest corrosion rate in total. The measured concentrations of Cu^{2+} and Fe^{3+} in cell medium extracts were much lower for CG/UFG Cu–5Fe than CG Cu, so that the cell compatibility of the alloys was much higher than the pure Cu. However, the concentration of Cu^{2+} in the extracts of CG Cu–5Fe was higher and the Fe^{3+} was lower comparing to these in the extracts of UFG Cu–5Fe. It could be the different corrosion process of the alloys in cell mediums with the presence of biological molecules, such as proteins. Under the simultaneous stimulations of low Cu^{2+} and high Fe^{3+}, the UFG Cu–5Fe alloy demonstrated better cell compatibility in 3 days while CG Cu–5Fe presented exceptionally high cell viability of HESC. For *In vivo*, both CG Cu–5Fe and UFG Cu–5Fe elicited sterile inflammatory responses in uterine cavity owing to foreign body response to the implantation of the cylindrical samples. However, the tissue damage induced by CG Cu–5Fe and UFG Cu–5Fe is significantly reduced compared to CG Cu, because of substantial decrease in Cu^{2+} release. In the later stages post-implantation, both CG Cu–5Fe and UFG Cu–5Fe groups also demonstrated enhanced damage repair capabilities, which probably because of simultaneously released Fe^{3+}. There are two main reasons. (1) Fe is the most abundant essential trace element in human body, approximately 4 g in total and 0.1 ~1 mmol/L in serum, playing a crucial physiological role [27]; (2) Commonly, the daily intake of Fe of most people is lower than the recommended dose [25], so that relatively high level of additional Fe^{3+} would lead to benefits rather than issues to health.

Our findings on the CG/UFG Cu–5Fe alloys showed superior performance in biocompatibility and also comparable contraceptive efficacy with other reported Cu, Cu alloys or Zn alloy for the application of IUD. The inhibition to the burst release of Cu^{2+} from the CG Cu–5Fe is much more effective than UFG Cu, UFG Cu–0.4Mg

Table 3
Comparisons in structure, composition, and properties of the CG Cu, CG-5Fe, UFG Cu-5Fe and other Cu, Zn alloys as the active material of IUD.

Alloys		CG Cu	CG Cu–5Fe	UFG Cu-5Fe	UFG Cu [21, 24]	UFG Cu–0.4Mg [24]	Cu-38 Zn [25]	Zn-1Cu [42]
Grain size (μm)		2–25	50–250	1–10	0.26–0.6	0.3	0.1–0.2	/
Second phase		/	Fe phase 5–10 μm	Fe phase 5–10 μm	/	/	~38.95 % Zn	/
Corrosion rate (μm/year)		61	73	54	31	27	14	53
Cu^{2+} release rate (μg/day)		251.4	43.9	207.2	112.3–146.2	76.6	12.2	67.0 (Zn^{2+})
Fe^{3+} release rate (μg/day)		/	627.3	316.0	/	/	6.9 (Zn^{2+})	/
[Cu^{2+}] (μg/mL)	DMEM/F12	192.1	13.7	1.6	153.2	116.6	22.6	0.021
	ECM	93.4	17.7	1.5	234.0	141.8	/	/
[Fe^{3+}] (μg/mL)	DMEM/F12	0.15	48.4	92.3	/	17.7 (Mg^{2+})	10.9 (Zn^{2+})	16.3 (Zn^{2+})
	ECM	0.12	53.7	82.2	/	21.1 (Mg^{2+})	/	/
Cell Viability	HEEC	~20 %	90.7 %	56.1 %	~12.5 %	~15 %	~32 %	~35 %
(Day 1, 100 % Extract)	HESC	~5 %	88.3 %	~80 %	~15 %	~15 %	~78 %	~60 %
	HUVEC	~15 %	50.4 %	72.7 %	~15 %	~20 %	/	/
Antifertility efficacy		100 %	100 %	100 %	100 %	100 %	100 %	100 %
Uterine Tissue Compatibility	3 days	No EECs, or glands	Partially intact EECs layer	Intact EECs layer & presence of glands	Microvesslesin sub-epithelial stroma	Almost no EECs	No EECs layer	Damaged endometrial, & no EECs layer
	14 days	Intensive inflammatory reaction	Self- recovery almost completed	Partially intact EECs layer	Squamous metaplasia present	Self- recovery partially completed	Self- recovery started	Self- recovery partially completed

EECs: endometrial epithelial cells.

and Zn–1Cu alloys, and it is also comparable to that of Cu–38 Zn. More prominently, the *in vitro* cell compatibility and *in vivo* tissue compatibility from our work present dramatically attractive performance. The contraceptive efficacy of all alloys is maintained at 100 %. Cu–5Fe alloys in both coarse and ultrafine structures are more promising to eliminate the adverse effects owing to the burst release of Cu^{2+} for Cu-IUD and will be a highly effective and compatible candidate as the active material for IUD.

5. Conclusions

In this work, we have produced a series of Cu-Fe alloys with different compositions, including 0.5 wt%Fe, 1 wt% and 5 wt%Fe. We also fabricated the ultrafine grained structures for these alloys via ECAP treatment, reducing the grain size from 50–200 μm to 1–10 μm. The systematic investigations on both the coarse grained and ultrafine grained Cu–Fe alloys demonstrated that Cu–5Fe alloy exhibited the best properties compared to the coarse grained Cu, which was attributed to the second phase of Fe embedded within Cu matrix. The corrosion behavior of the coarse grained Cu–5Fe alloy in the SUF differed from that of the CG Cu as a galvanic cell (Cu–Fe) formed with 5 wt% Fe, with Fe corroding earlier than Cu. This inhibited the burst release of the Cu^{2+} substantially while simultaneously released the Fe^{3+} at a high rate. As the most abundant essential trace element in human body, the early and substantial release of Fe^{3+} significantly improved the cell compatibility of the Cu–5Fe alloys. The Cu–5Fe alloy maintained the high contraceptive efficiency with greatly reduced adverse effects on the uterine tissue. Therefore, the Cu–5Fe alloy can be used as a more active and biocompatible material for the Cu-IUD.

Declaration of competing interest

The authors declare that they have no known competing financial interests or personal relationships that could have appeared to influence the work reported in this paper.

CRediT authorship contribution statement

Lijun Yang: Writing – original draft, Investigation, Formal analysis, Data curation, Conceptualization. **Guo Bao:** Writing – original draft, Investigation, Data curation, Conceptualization. **Cancan Yao:** Methodology, Investigation. **Tian Diao:** Methodology, Investigation. **Zhenning Su:** Methodology, Investigation. **Tingting Liu:** Methodology, Investigation. **Guannan Li:** Methodology, Investigation. **Gonglei Wang:** Methodology, Investigation. **Xihua Chen:** Methodology, Investigation. **Xiangbo Xu:** Methodology, Investigation. **Bing Sun:** Methodology, Investigation. **Xiaoxue Xu:** Writing – review & editing, Validation, Supervision, Methodology, Formal analysis, Conceptualization. **Bin He:** Writing – review & editing, Supervision, Resources, Funding acquisition, Conceptualization. **Yufeng Zheng:** Writing – review & editing, Supervision, Resources, Project administration, Conceptualization.

Acknowledgment

Lijun Yang and Guo Bao contributed equally to this work. This work was supported by National Natural Science Foundation of China (Grant no. 52171237) and the Non-Profit Central Research Institute Fund of National Research Institute for Family Planning (Grant no. 2022GJM03). This project was partially supported by the Cross-Faculty Collaborative Grant of University of Technology Sydney (PRO24-18872). We would like to acknowledge the Laboratory Animal Centre, National Research Institute for Family Planning, Beijing for the animal experiment support and also the Microscopy Analysis Unit at the University of Technology Sydney for microstructure analysis.

Supplementary materials

Supplementary material associated with this article can be found, in the online version, at doi:10.1016/j.actbio.2024.09.022.

References

[1] K.M. Curtis, J.F. Peipert, Long-acting reversible contraception, N. Engl. J. Med. 376 (5) (2017) 461–468.
[2] M.K. Findley, E.E. Levi, M.V. Dragoman, Intrauterine devices and contraceptive implants: overview of options and updates on method use, Curr. Obstet. Gynecol. Rep. 6 (2) (2017) 85–93.
[3] J. Krashin, J.H. Tang, S. Mody, L.M. Lopez, Hormonal and intrauterine methods for contraception for women aged 25 years and younger, Cochrane Database Syst. Rev. 2015 (8) (2015) Cd009805.
[4] J.A. Zipper, H.J. Tatum, L. Pastene, M. Medel, M. Rivera, Metallic copper as an intrauterine contraceptice adjunct to the "T" device, Am. J. Obstet. Gynecol. 105 (8) (1969) 1274–1278.
[5] M.E. Ortiz, H.B. Croxatto, C.W. Bardin, Mechanisms of action of intrauterine devices, Obstet. Gynecol. Surv. 51 (12 Suppl) (1996) S42–S51.
[6] M.E. Ortiz, H.B. Croxatto, Copper-T intrauterine device and levonorgestrel intrauterine system: biological bases of their mechanism of action, Contraception 75 (6 Suppl) (2007) S16–S30.
[7] Z. Chen, H. Meng, G. Xing, C. Chen, Y. Zhao, G. Jia, T. Wang, H. Yuan, C. Ye, F. Zhao, Z. Chai, C. Zhu, X. Fang, B. Ma, L. Wan, Acute toxicological effects of copper nanoparticles *in vivo*, Toxicol. Lett. 163 (2) (2006) 109–120.
[8] J.P. Carrascosa, D. Cotán, I. Jurado, M. Oropesa-Ávila, P. Sánchez-Martín, R.F. Savaris, J. Tan, J.A. Sánchez-Alcázar, S.L. Tan, J.A. Horcajadas, The effect of copper on endometrial receptivity and induction of apoptosis on decidualized human endometrial stromal cells, Reprod. Sci. 25 (7) (2018) 985–999.
[9] R.L. Brinster, P.C. Cross, Effect of copper on the preimplantation mouse embryo, Nature 238 (5364) (1972) 398–399.
[10] S. Fadiloglu, B. Dilbaz, E. Fadiloglu, S. Dilbaz, Relationship between copper IUD complications and ultrasonographic findings, Arch. Gynecol. Obstet. 297 (4) (2018) 989–996.
[11] L. Li, J. Li, N. Li, Y. Zhang, X. Feng, Analysis of the reason of abnormal uterine bleeding induced by copper corrosion of IUD Cu, Clin. Exp. Obstet. Gynecol. 43 (6) (2016) 883–886.
[12] J. Zhou, X. Tan, X. Song, K. Zhang, J. Fang, L. Peng, W. Qi, Z. Nie, M. Li, R. Deng, C. Yan, Temporal trends of copper-bearing intrauterine device discontinuation: a population-based birth-cohort study of contraceptive use among rural married women in China, Asia Pac. J. Public Health 27 (2) (2015) Np2433-42.
[13] L. Jinying, L. Ying, G. Xuan, G. Yanli, L. Jianping, Investigation of the release behavior of cupric ion for three types of Cu-IUDs and indomethacin for medicated Cu-IUD in simulated uterine fluid, Contraception 77 (4) (2008) 299–302.
[14] J. Li, J. Suo, X. Huang, C. Ye, X. Wu, Comparison of the release behaviors of cupric ions from metallic copper and a novel composite in simulated body fluid, J. Biomed. Mater. Res. B Appl. Biomater. 85 (1) (2008) 172–179.
[15] J. Li, J. Suo, X. Huang, L. Jia, Study on a novel copper-containing composite for contraception, Contraception 79 (6) (2009) 439–444.
[16] J. Li, J. Suo, X. Huang, C. Ye, X. Wu, Release behavior of copper ion in a novel contraceptive composite, Contraception 76 (3) (2007) 233–237.
[17] W. Zhang, X. Xia, C. Qi, C. Xie, S. Cai, A porous Cu/LDPE composite for copper-containing intrauterine contraceptive devices, Acta Biomater. 8 (2) (2012) 897–903.
[18] S. Cai, X. Xia, C. Xie, Corrosion behavior of copper/LDPE nanocomposites in simulated uterine solution, Biomaterials 26 (15) (2005) 2671–2676.
[19] L. Sun, X.B. Huang, J.P. Suo, B.L. Fan, Z.L. Chen, W.X. Yang, J. Li, Biological evaluation of a novel copper-containing composite for contraception, Fertil. Steril. 95 (4) (2011) 1416–1420.
[20] K. Tian, C. Xie, X. Xia, Chitosan/alginate multilayer film for controlled release of IDM on Cu/LDPE composite intrauterine devices, Colloids Surf. B Biointerfaces 109 (2013) 82–89.
[21] X.X. Xu, F.L. Nie, Y.B. Wang, J.X. Zhang, W. Zheng, L. Li, Y.F. Zheng, Effective inhibition of the early copper ion burst release with ultra-fine grained copper and single crystal copper for intrauterine device application, Acta Biomater. 8 (2) (2012) 886–896.
[22] D.M. Bastidas, B. Valdez, M. Schorr, J.M. Bastidas, Corrosion of copper intrauterine devices: review and recent developments, Corros. Rev. 37 (4) (2019) 307–320.
[23] Q. Fan, G. Bao, D. Ge, K. Wang, M. Sun, T. Liu, J. Liu, Z. Zhang, X. Xu, X. Xu, B. He, J. Rao, Y. Zheng, Effective easing of the side effects of copper intrauterine devices using ultra-fine-grained Cu-0.4Mg alloy, Acta Biomater. 128 (2021) 523–539.
[24] K. Wang, G. Bao, Q. Fan, L. Zhu, L. Yang, T. Liu, Z. Zhang, G. Li, X. Chen, X. Xu, X. Xu, B. He, Y. Zheng, Feasibility evaluation of a Cu-38 Zn alloy for intrauterine devices: *in vitro* and *in vivo* studies, Acta Biomater. 138 (2022) 561–575.
[25] Y. Liu, Y. Zheng, X.-H. Chen, J.-A. Yang, H. Pan, D. Chen, L. Wang, J. Zhang, D. Zhu, S. Wu, K.W.K. Yeung, R.-C. Zeng, Y. Han, S. Guan, Fundamental theory of biodegradable metals—definition, criteria, and design, Adv. Funct. Mater. 29 (18) (2019) 1805402.
[26] J. Emsley, Nature's Building Blocks: An A–Z Guide to the Elements, Oxford University Press, Oxford, UK, 2011.
[27] Z.Y.X. Lyu, G. Wang, Biology of Elements (in Chinese), University of Science and Technology of China Press, Hefei, China (2011).
[28] J.L.S.S. Gropper, Advanced Nutrition and Human Metabolism, Y. Cossio, S. Gropper, J.L. Smith (Eds.), 2013.
[29] J.F. Zheng, H. Qiu, Y. Tian, X.Y. Hu, T. Luo, C. Wu, Y. Tian, Y. Tang, L.F. Song, L. Li, L. Xu, B. Xu, R.L. Gao, Preclinical evaluation of a novel sirolimus-eluting iron bioresorbable coronary scaffold in porcine coronary artery at 6 months, JACC Cardiovasc. Interv. 12 (3) (2019) 245–255.
[30] Q.Z.L. Shi, Cheng Luo, Hao Chen, Jibiao Yang, Xiaodong Zhang, Xianbin Li, Effect of copper content and sintering temperature on friction and wear properties of powder-metallurgical Fe-Cu based composites, Chin. J. Mater. Res. 34 (2) (2020) 137–150.
[31] C. Alonso, E. Casero, E. Román, S.F.P. Campos, M.F.L. de Mele, Effective inhibition of the early copper ion burst release by purine adsorption in simulated uterine fluids, Electrochim. Acta 189 (2016) 54–63.
[32] J.M. Bastidas, E. Cano, N. Mora, Copper corrosion-simulated uterine solutions, Contraception 61 (6) (2000) 395–399.
[33] M.D. Pereda, S.B. Farina, M. Fernández Lorenzo, Is the early fragmentation of intrauterine devices caused by stress corrosion cracking? Acta Biomater. 5 (8) (2009) 3240–3246.
[34] N. Mora, E. Cano, E.M. Mora, J.M. Bastidas, Influence of pH and oxygen on copper corrosion in simulated uterine fluid, Biomaterials 23 (3) (2002) 667–671.
[35] X. Zhou, Y. Li, X. Jiang, L. Qiu, J. Liu, Release of copper and indomethacin from intrauterine devices immersed in simulated uterine fluid, Eur. J. Contracept. Reprod. Health Care 15 (3) (2010) 205–212.
[36] G. Lewis, R. Vejerla, S. Mishra, One equivalent electrical circuit is applicable to model the interface between the passive surface layer on an orthopaedic alloy and a biosimulating aqueous solution, Biomed. Mater. Eng. 17 (2) (2007) 97–108.
[37] S. Colin, E. Bêche, R. Berjoan, H. Jolibois, A.A.A. Chambaudet, An XPS and AES study of the free corrosion of Cu-, Ni- and Zn-based alloys in synthetic sweat, Corros. Sci. 41 (1999) 1051–1065.
[38] Q. Guo, H. Huang, L. Gui, Y. Xie, Y. Tang, Studies of CuCl/γ-Al_2O_3 by XPS, SSIMS AND ISS, Acta Physico-Chim. Sin. 3 (1987) 389–394.
[39] N.S. McIntyre, M.G. Cook, X-ray photoelectron studies on some oxides and hydroxides of cobalt, nickel, and copper, Anal. Chem. 47 (13) (1975) 2208–2213.
[40] T. Jin, W. Zhang, N. Li, X. Liu, L. Han, W. Dai, Surface characterization and corrosion behavior of 90/10 copper-nickel alloy in marine environment, Materials (Basel) 12 (11) (2019) 1869.
[41] M.C. Biesinger, B.P. Payne, A.P. Grosvenor, L.W.M. Lau, A.R. Gerson, R.S.C. Smart, Resolving surface chemical states in XPS analysis of first row transition metals, oxides and hydroxides: Cr, Mn, Fe, Co and Ni, Appl. Surf. Sci. 257 (7) (2011) 2717–2730.
[42] C. Zhang, N. Xu, B. Yang, The corrosion behaviour of copper in simulated uterine fluid, Corros. Sci. 38 (4) (1996) 635–641.
[43] H. Xue, N. Xu, C. Zhang, Corrosion behavior of copper in a copper bearing intrauterine device in the presence of indomethacin, Contraception 57 (1) (1998) 49–53.
[44] S.A. Campbell, G.J.W. Radford, C.D.S. Tuck, B.D. Barker, Corrosion and galvanic compatibility studies of a high-strength copper-nickel alloy, Corrosion 58 (2002) 57–71.
[45] R. Babić, M. Metikoš-Huković, M. Lončar, Impedance and photoelectrochemical study of surface layers on Cu and Cu–10Ni in acetate solution containing benzotriazole, Electrochim. Acta 44 (14) (1999) 2413–2421.
[46] E.M. Sherif, S.-M. Park, 2-Amino-5-ethyl-1,3,4-thiadiazole as a corrosion inhibitor for copper in 3.0% NaCl solutions, Corros. Sci. 48 (12) (2006) 4065–4079.
[47] D.M. Bastidas, B. Valdez, M. Schorr, J.M. Bastidas, Corrosion of copper intrauterine devices: review and recent developments, Corros. Rev. 37 (2019) 307–320.